 doi:10.20944/preprints202101.0255.v1

Article

Canopy top, height and photosynthetic pigment estimation using Parrot Sequoia multispectral imagery and the Unmanned Aerial Vehicle (UAV)

Veronika Kopačková-Strnadová [1,*], Lucie Koucká [1], Jan Jelének [1], Zuzana Lhotáková [2] and Filip Oulehle [1]

[1] Czech Geological Survey, Klárov 3, Prague 1, 11821, Czech Republic; veronika.kopackova@seznam.cz
[2] Charles University, Faculty of Science, Department of Experimental Plant Biology, Viničná 5, Prague 2, 12844 ; zuza.lhotak@seznam.cz
* Correspondence: veronika.kopackova@seznam.cz; Tel.: +420-257-089-481 (V.K.-S.)

Abstract: Remote sensing is one of the modern methods that have significantly developed over the last two decades and nowadays provides a new means for forest monitoring. High spatial and temporal resolutions are demanded for accurate and timely monitoring of forests. In this study multi-spectral Unmanned Aerial Vehicle (UAV) images were used to estimate canopy parameters (definition of crown extent, top and height as well as photosynthetic pigment contents). The UAV images in Green, Red, Red-Edge and NIR bands were acquired by Parrot Sequoia camera over selected sites in two small catchments (Czech Republic) covered dominantly by Norway spruce monocultures. Individual tree extents, together with tree tops and heights, were derived from the Canopy Height Model (CHM). In addition, the following were tested i) to what extent can the linear relationship be established between selected vegetation indexes (NDVI and $NDVI_{red\ edge}$) derived for individual trees and the corresponding ground truth (e.g., biochemically assessed needle photosynthetic pigment contents), and ii) whether needle age selection as a ground truth and crown light conditions affect the validity of linear models. The results of the conducted statistical analysis show that the two vegetation indexes (NDVI and $NDVI_{red\ edge}$) tested here have a potential to assess photosynthetic pigments in Norway spruce forests at a semi-quantitative level, however the needle-age selection as a ground truth was revealed to be a very important factor. The only usable results were obtained for linear models when using the 2nd year needle pigment contents as a ground truth. On the other hand, the illumination conditions of the crown proved to have very little effect on the model's validity. No study was found to directly compare these results conducted on coniferous forest stands. This shows that there is a further need for studies dealing with a quantitative estimation of the biochemical variables of nature coniferous forests when employing spectral data acquired by the UAV platform at a very high spatial resolution.

Keywords: UAV; Parrot Sequoia multispectral camera; photosynthetic pigments; Norway spruce; forest; linear models; ground truth; needle age; crown detection

1. Introduction

Forests play a significant role in the Earth's ecosystems and contribute greatly to reducing adverse climate change impacts. They provide a natural environment for many species of animals and plants, represent a significant carbon sink and support an effective hydrological cycle. In addition, forests serve as an important source of timber and other non-wood materials [1,2]. Due to the aforementioned functions of forests and the increasing level of damage they suffer, at the beginning of the 1980s forest health and the sustainability of their ecosystems became a highly discussed topic for politicians, the public and scientists [3].

In Europe, temperate forests are mainly affected by climate change and air pollution, which was particularly significant in the study area too [4,5]. During the 20th century the region on the Czech,

 doi:10.20944/preprints202101.0255.v1

Polish and German borders was influenced by extensive coal mining which was linked to large emissions of SO_2 and NOx from power plants [6,7]. In order to monitor the process of ecosystem recovery after the reduction in pollution that started in the 1980s and accelerated in the 1990s, the GEOMON network of small catchments was initiated across the Czech Republic. Since 1993, when the GEOMON network began, the data collected from observations of these catchments have been used for many studies [7,8] corresponding mainly to catchment biogeochemistry (e.g., [6,9–13]). The recent study published by Švik et al. [7] supplied the aforementioned research based on field observations using remote sensing methods which have been focused on in this study.

Remote sensing techniques have been frequently used to study forest areas for multiple purposes over the last decade. They have been proven to be less costly and time-consuming alternatives to ground level research [14]. Satellite and aerial imagery have offered an opportunity to investigate forests at the regional scale, for example to estimate forest biomass, monitor forest cover changes or classify types of biome [15–18]. The usage of airborne multispectral and hyperspectral sensors has led to closer forest observation, such as the classification of tree species, monitoring forest health or estimating chlorophyll content [19–24]. The newly developed Unmanned Aerial Vehicles (UAV) complement the established remote sensing (RS) methods. UAVs have increased the number of benefits such as acquiring extreme high-spatial resolution data, flexibility in usage and over time, and the capacity to carry various sensors such as a multispectral camera to observe vegetational health [25,26].

Most of the studies use a combination of UAV complemented by a multispectral sensor to analyse agriculture crops for precision farming (e.g. tomato, vineyard or wheat production) where they usually employ Vegetation Indices (VIs) such as the Normalized Difference Vegetation Index (NDVI), the Green Normalized Difference Vegetation Index (GNDVI) or the Soil Adjusted Vegetation Index (SAVI) to monitor crop health [27–30]. Authors monitoring vineyards described the use of multispectral and thermal sensors in combination to obtain additional information about crop water status [31,32]. Despite the high potential of UAVs, not many studies have dedicated an analysis of multispectral data during forest observation. For instance, Dash et al. [33] simulated disease symptoms on *Pinus radiata* trees through herbicide application to test the sensitivity of spectral indices based on repeating UAV multispectral data acquisition. Minařík and Langhammer [34] suggested the use of VIs to classify forest disturbance on a Norway spruce monoculture to identify bark beetle infestation. A more sophisticated technique to detect symptoms caused by bark beetle attack was described by Näsi et al. [35] who employed k-nearest neighbour classification on 3D hyperspectral data. Moreover, the comparison of a pixel- and object-based classification of UAV multispectral data for coniferous tree species in Canada was discussed in Franklin [36] where automated tree crown delineation was also applied. All these studies listed above deal with qualitative forest classifications, so a need for quantitative approaches, focusing on forest biochemical variable estimations employing UAV-based multispectral sensing, is clearly demanded.

For such quantitative spectral-based approaches, that employ very high-spatial resolution data, an accurate definition of the extent of individual trees is a crucial task. Delineation of a tree crown boundary has been studied before and several approaches to detect individual trees have been published. Lim et al. [37] applied a segmentation method to a combination of the RGB orthoimage and the Canopy Height Model (CHM) obtained by UAV. A similar approach using multispectral data instead was described in Díaz-Varela et al. [38]. A popular technique is hydrological terrain analysis - watershed algorithm, where the inverse CHM is delineated by the watershed algorithm where catchment basins represent individual trees and holes substitute tree peaks [15,39–41]. Among the recent methods are the LiDAR point cloud segmentation, which achieves highly accurate results. This technique uses a regional growth principle where the highest vertex point (tree top) is defined as the start point. The region is iteratively growing from the tree top downwards in a range of set threshold values to delineate the tree crown [39,42,43].

This study tested if a UAV equipped with a multispectral camera can be employed for photosynthetic pigment estimation in mature coniferous trees. Two small catchments (part of the GEOMON network in Czech Republic) inhabited by Norway spruce monocultures were selected based on relatively close spatial proximity, alongside differences in parent material, which

Preprints (www.preprints.org) | NOT PEER-REVIEWED | Posted: 13 January 2021 doi:10.20944/preprints202101.0255.v1

significantly influenced nutrient availability for forest ecosystems. The research further focused on the following issues:

- An accurate definition of the individual tree extents (crown delineation) and derivation of other parameters such as tree top and height using the UAV-based multispectral data.
- Testing if linear relationship can be established between selected vegetation indices (NDVI and $NDVI_{red\ edge}$) derived for individual trees and the corresponding ground truth (e.g., biochemically assessed needle photosynthetic pigment contents).
- Testing if the needle age selection as ground truth affects the validity of the linear models.
- Testing if the tree crown light conditions affect the validity of the linear models.

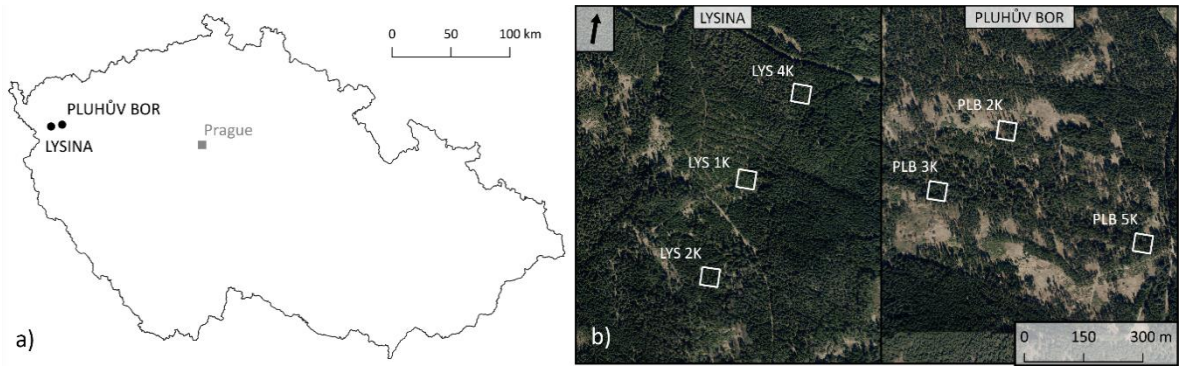

Figure 1. Location of the test sites Pluhův Bor and Lysina in the Czech Republic, Europe: (a) the test sites displayed on a map of the Czech Republic; (b) maps of the Lysina and Pluhův Bor catchments with tree stands highlighted; an Orthophoto of the Czech Republic in the background [44].

2. Materials and Methods

2.1. Test sites

Two test sites representing rural mountainous landscapes in the western part of Bohemia were selected - Lysina (LYS) and Pluhův Bor (PLB) (Figure 1). These two catchments have been part of the European network - GEOMON established in 1993 to assess changes in precipitation and stream chemistry after reducing pollution in Eastern Europe. The selected catchments were heavily affected by acid pollution during the 20th century. Nowadays, both sites are part of the Slavkov Forest Protected Landscape Area. The vegetation cover consists mostly of managed Norway spruce monocultures [10] which are situated around 800 m a. s. l. The main difference between these two sites is the lithology and soil type as well as the forest age. Detailed catchment characteristics are given in Table 1 and 2.

Preprints (www.preprints.org) | NOT PEER-REVIEWED | Posted: 13 January 2021 doi:10.20944/preprints202101.0255.v1

Table 1. Characteristics of selected catchments: Lysina and Pluhův Bor [10].

Site	Bedrock	Soils	Elevation (m a. s. l.)	Forest age (year range)	Spruce forest (ha)	Broadleaf forest (ha)	Non-forested area (ha)
LYS	Granite	Cambisols, Podzols	880	12–53	27	0.0	0.4
PLB	Serpentinite	Magnesic Cambisols, Stagnic–Magnesic Cambisols, Magnesic Gleysols	755	41–129	18	0.0	4.0

Table 2. Tree ages at the two catchments selected in this study.

Test site	Average age	Min age	Max age
LYS 1K	14	12	17
LYS 2K	16	15	18
LYS 4K	47	44	53
PLB 2K	120	109	129
PLB 3K	72	70	74
PLB 5K	47	41	50

2.2. In-situ ground truth

In this study three tree stands were selected in the LYS catchment (LYS 1K, LYS 2K, LYS 4K) and three stands in the PLB catchment (PLB 2K, PLB 3K, PLB 5K), these stands were the object of previous long-term research, thus the soil conditions were known as well as tree height information which was measured in-situ and modelled using the LiDAR data [45].

At each stand three representative trees were selected and branch samples were collected by a climber from the sunlit crown part one day before the UAV-based data were acquired (August 2018). The needle age was identified and three different age classes were sampled: 1st, 2nd and a mixed sample of 4th year and older needles (hereinafter referred to as 4th year for simplicity) [46]. The needles were cooled and immediately transported to the laboratory where they were kept at a stable temperature at -20° C until further processing. Photosynthetic pigments - chlorophyll a, b and total carotenoids - were extracted in dimethylformamide following the procedures described in detail by Porra et al. [47] and then spectrophotometrically determined [48]. Mean pigment contents for both sites are summarized in Table 3.

Table 3. Mean contents of photosynthetic pigments based on in-situ needle samples for both catchments.

	Catchment	All needles	1st year needles	2nd year needles	4+years needles
Total Chlorophyll (ug . cm-2)	Lysina (LYS)	52.580	35.756	56.055	65.399
	Pluhův Bor (PLB)	44.425	31.148	43.895	57.172
Chlorophyll a (ug . cm-2)	Lysina (LYS)	37.939	26.124	40.679	46.637
	Pluhův Bor (PLB)	32.071	22.810	31.989	40.672
Chlorophyll b (ug . cm-2)	Lysina (LYS)	14.641	9.631	15.373	18.761
	Pluhův Bor (PLB)	12.354	8.343	11.904	16.500
Carotenoids (ug . cm-2)	Lysina (LYS)	6.724	4.400	7.018	8.602
	Pluhův Bor (PLB)	5.596	3.451	5.284	7.591

Preprints (www.preprints.org) | NOT PEER-REVIEWED | Posted: 13 January 2021 doi:10.20944/preprints202101.0255.v1

2.3. UAV data acquisition

2.3.1. Equipment

In this experiment, an unmanned aerial vehicle DJI Phantom 4 (SZ DJI Technology Co., Ltd. [49]) was employed (Figure 2b). It is a widely used quadcopter weighing 1380 g with an RGB camera in 4K (4096 x 2160 px) [50]. The UAV was complemented by a multispectral camera Parrot Sequoia scanning system (senseFly Inc. [51]). The camera was specially designed to support vegetation studies therefore besides Red and Green bands there is a band placed in the Red edge region as well as one band in the Near infrared (NIR) (Table 4).

Table 4. Overview of a Parrot Sequoia spectral band setting.

Band name	Spectral Range (nm)	Central Wavelength (nm)
Green	530 – 570	550
Red	640 – 680	660
Red edge (RE)	730 – 740	735
Near infrared (NIR)	770 - 810	790

The Parrot Sequoia consists of two parts - the main camera and a sunshine sensor calibrating the measured spectral radiation by the main sensor. These two parts of the multispectral camera were attached to the drone by mounts designed by the CGS team (Figure 2a). The 3D models of mounts were created in CAD software. It was important to make a free space for the GPS sensor to ensure good signal reception. The holder for the sunshine sensor had to be placed in a manner so as not to have any contact with the propellers (Figure 2a). The mounts were printed using the Prusa i3 3D printer (Prusa Research a.s. [52]).

2.3.2. Data acquisition

The RGB and Parrot Sequoia multispectral data were obtained for both test sites. The flights were made on 6 and 7 August 2018, between 11 am and 3 pm to ensure the multispectral camera captured the required maximum reflected sunlight and to eliminate shadows. Prior to data acquisition, a flight path was planned in the flylitchi.com web tool (Figure 2c), which was connected to the litchi android application (VC Technology Ltd. [53]) controlling the UAV. Areas of 40 x 40 m were defined to cover the tree groups and their surroundings. All the flight paths covering the area of interest were planned in a north-south direction and in a way so the parallel scanning lines would reach 70% of the side overlap to ensure errorless image mosaicking when creating photogrammetric products. Flight height was set up according to the highest terrain point (40 - 70 m above ground level) and was 25-30 m above the treetops. UAV speed was set at 3.6 km/h to ensure well-focused images were recorded. Sequences of images were recorded every 2 seconds (s) with 95% overlap in the direction of the flight. According to flight height, the resulting spatial resolution of RGB imagery varied between 1.1 - 1.9 cm/px and 3.76 - 6.59 cm/px for multispectral imagery, respectively.

Regarding multispectral data calibration, images of the calibrated reflectance panel were acquired before and after each flight. The same routine was used for each flight - the calibration target (Aironov) was placed on the ground and the UAV was held above the panel always keeping the same position - the Sun was behind the UAV, so no reflection and shadow was affecting the panel as this was recommended by the manufacturer. The same rules were applied to the other cameras (e.g., [54]).

GPS data from DJI Phantom 4 and Parrot Sequoia camera were used to reference the resulting orthomosaics into the coordinate system (WGS 84 / UTM 33N). The imaging data (RGB and multispectral bands) were processed in Agisoft Metashape software (Agisoft LLC [55]), which allowed orthomosaics (RGB and multispectral) and digital surface models (DSMs) to be created using the structure from motion method [56]. The multispectral data calibration was made automatically by the Agisoft Metashape software which detected the images of the calibrated panel by the QR code in it as described in [57].

Preprints (www.preprints.org) | NOT PEER-REVIEWED | Posted: 13 January 2021 doi:10.20944/preprints202101.0255.v1

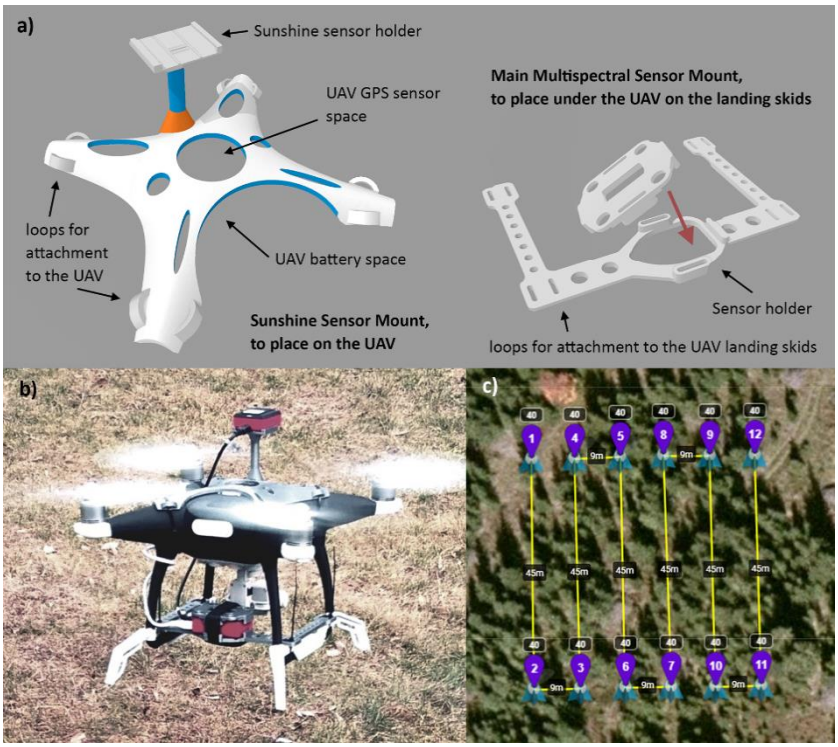

Figure 2. UAV equipment used in this study: (a) 3D models of the mounts designed for the Parrot Sequoia multispectral camera; (b) DJI Phantom 4 quadcopter with attached Parrot Sequoia camera; (c) planned flight path in the flylitchi.com web tool.

2.4. Tree height, crown and top detection

Tree height detection was based on the Canopy Height Model (CHM) described as the difference between treetop elevation and the underlying ground-level elevation [58]. In this study, the 5th Digital Elevation Model (DEM) generation (DMR 5G; [44,59]) was used as a source of ground-level information while treetop information was obtained from the digital surface model (DSM) obtained from the Parrot Sequoia camera multispectral images (Seq DSM):

$$\text{CHM} = \text{Seq DSM} - \text{DMR 5G} \quad (1)$$

First, the DMR 5G data (original spatial resolution 0.5 m) was resampled to a Seq DSM spatial resolution of 16 - 25 cm (Table 6), and Seq DSM was calibrated by DMR 5G elevation to obtain proper results. The calibration was performed at each site by extracting the average heights from the Seq DSM of a clearing or forest path then it was possible to compare this height value with the average site altitude derived from the DMR 5G. The elevation of the Seq DSM was then corrected by this difference.

To derive tree tops, the following procedure was employed. Focal statistics was employed to the CHM raster to get rid of noisy pixels and a new dataset was created (CHMfoc). According to the empirical tests carried out, the best results were achieved when using the maximum value and a 5x5-pixel window [60]. A window with a smaller size caused frequent double peak detection. On the other hand, a bigger window did not identify a sufficient number of tree peaks. Tree tops were detected by identifying the local maxima in the CHMfoc raster. The representative pixels for the highest CHMfoc values were then identified in the original CHM raster, as it was important to keep the original pixel positions and values and the treetop point layer was derived [40]. The tree height detection workflow is shown in Figure 3.

Preprints (www.preprints.org) | NOT PEER-REVIEWED | Posted: 13 January 2021 doi:10.20944/preprints202101.0255.v1

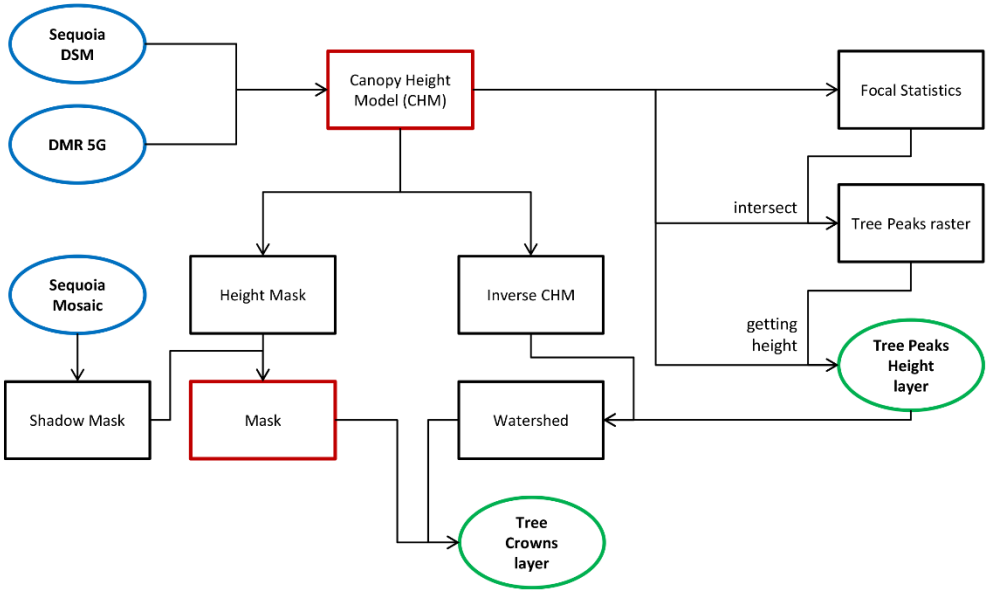

Figure 3. Workflow used in this study to detect tree height, crown and top.

To delineate the tree crowns the workflow described by Jaakkola et al. [41] was followed, which used watershed analysis to identify tree crown borders using the CHM derived from UAV-based laser scanning. First, inverse CHM (iCHM) was created where trees were visualized as depressions and treetops represented the lowest points in the digital elevation model:

$$iCHM = CHM * (-1) \quad (2)$$

The iCHM, together with the tree peak layer representing pour points, were used to compute watershed regions. The watershed analysis showed good results even in the case of splitting two or multiple nearby standing trees (Figure 4a).

Tree borders in places with no connection to another tree crown were defined using a height mask (Figure 4b) allowing the space under the tree crowns to be removed. The height mask was created by excluding such areas where the CHM altitude was at least 3 m lower than the actual lowest detected tree height (Table 5).

Consequently, to visualise only sunlit crown parts convenient for the following multispectral analyses, the shadow mask was derived by thresholding the Red band of the multispectral mosaic (Seq Mosaic) and selecting those values lower than 0.04 [61]. In the next step, the height mask was merged with the shadow mask (Figure 4c). The final tree crown boundaries were obtained by applying the merged mask to the watershed layer (Figure 4d), as a result the individual tree crowns were extracted.

Table 5. Height mask thresholds used in this study.

Test site	Height mask threshold [m]
LYS 1K	3
LYS 2K	5
LYS 4K	20
PLB 2K	19
PLB 3K	13
PLB 5K	18

Preprints (www.preprints.org) | NOT PEER-REVIEWED | Posted: 13 January 2021 doi:10.20944/preprints202101.0255.v1

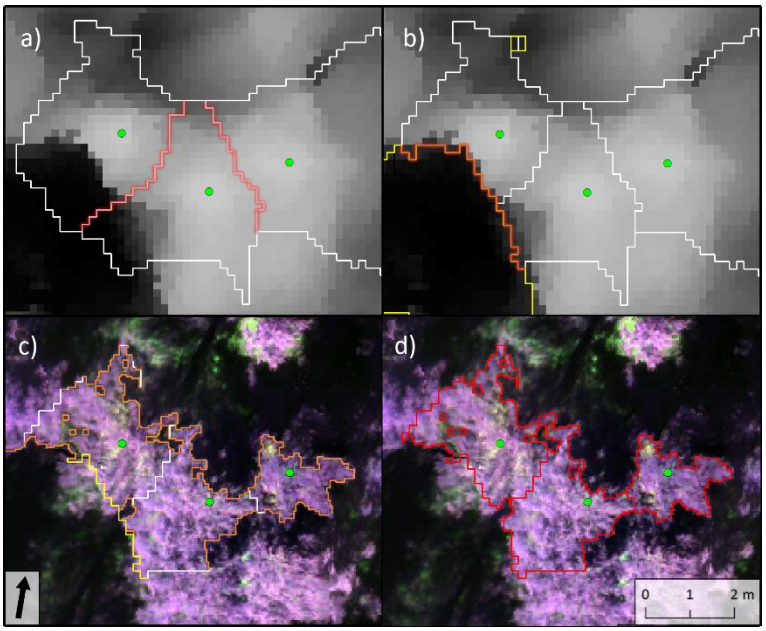

Figure 4. An example of tree crown detection (tree peaks visualized by green dots): (a) watersheds surrounding treetops (white line) split nearby trees - the borders are highlighted in red; DSM on the background; (b) the height mask (yellow line) cuts one side of the tree crowns in a place with a high altitude difference (red highlight); (c) the shadow mask (orange line) reduces the dark parts of tree crowns and completes the tree crown borders; multispectral imagery from the Parrot Sequoia sensor on the background (false-colour composition: Green, Red, Red edge); (d) final result of tree crown detection.

2.5. Multispectral data processing

As was mentioned, the Parrot Sequoia camera captures 4-band images (Green, Red, Red edge and Near infrared), which were designed specifically for vegetation analysis (Table 4). These bands allow the Normalized Difference Vegetation Index (NDVI) [62] to be computed, which is a universal vegetation index, but also, more importantly, they allow modification of NDVI when using the Red edge band instead of the Red band. Red Edge Normalized Difference Vegetation Index ($NDVI_{red\ edge}$) has been used to assess vegetation stress [63], as the stress directly affects the wavelength position of the red-edge inflexion point on the electromagnetic spectrum [64,65]. $NDVI_{red\ edge}$ index is defined as:

$$\frac{NIR-RE}{NIR+RE}, \quad (3)$$

where *NIR* is the Near infrared band and *RE* is the Red edge band of the Parrot Sequoia camera. Individual tree masks derived from the Sequoia image data (described in detail in Section 2.4) were used to find the relationship between the photosynthetic pigment contents and the two VIs (NDVI and $NDVI_{red\ edge}$),.

As the UAV-based imaging data are provided at exceptionally high spatial resolution, the intention was to test whether crown illumination affects the estimation of the photosynthetic pigments. Therefore, the tree crowns derived from the iCHM (Section 2.4) were classified into two classes - class 1 representing the part of the crown which received higher illumination and class 2, which represents the part of the crown that receives lower illumination compared to class 1. To create these two classes Principal component analysis (PCA) transformation [66] was employed. The first three PCA components were then classified using ISODATA (Iterative Self-Organizing Data Analysis Technique; [67]) the unsupervised classifier placing them into two classes. The classification results were visually assessed - compared to the orthophotomosaics (RGB and multispectral) - and it was concluded that using the above-described method it was possible to differentiate between the higher and lower-illuminated parts of a crown. Figure 5 gives an example of tree No. 22 (PLB 5K stand), the distribution of class 1 and 2 within the tree crown and the average

Preprints (www.preprints.org) | NOT PEER-REVIEWED | Posted: 13 January 2021 doi:10.20944/preprints202101.0255.v1

reflectance derived for these two classes. Three scenarios have been defined for further statistical analysis (Figure 6):

- Scenario 1: all the pixels representing the whole tree crown have been included.
- Scenario 2: pixels representing the higher-illumination top part of the crown have been included.
- Scenario 3: pixels representing the lower-illumination part of the crown have been included.

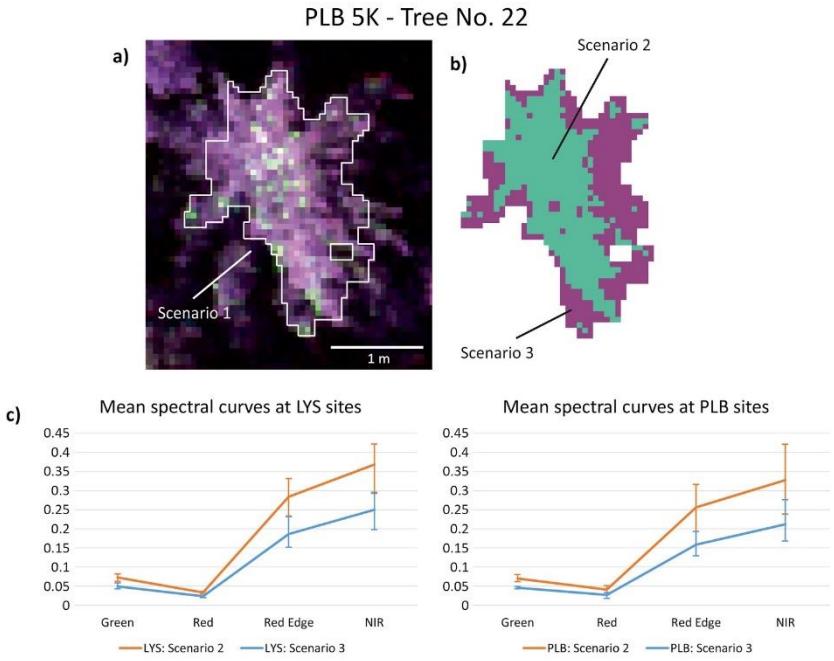

Figure 5. Scheme of Tree No. 22 at the PLB-5K stand showing (a) Parrot Sequoia multispectral data in band combination 4-2-1 (NIR, Red, Green) corresponding to Scenario 1; (b) Two classes representing Scenario 2 (the top higher-illumination part of the crown) and Scenario 3 (the lower-illumination part of the crown); (c and d) Mean reflectance per different illumination scenarios. Vertical bars represent minimum and maximum values for each band and scenario.

Preprints (www.preprints.org) | NOT PEER-REVIEWED | Posted: 13 January 2021 doi:10.20944/preprints202101.0255.v1

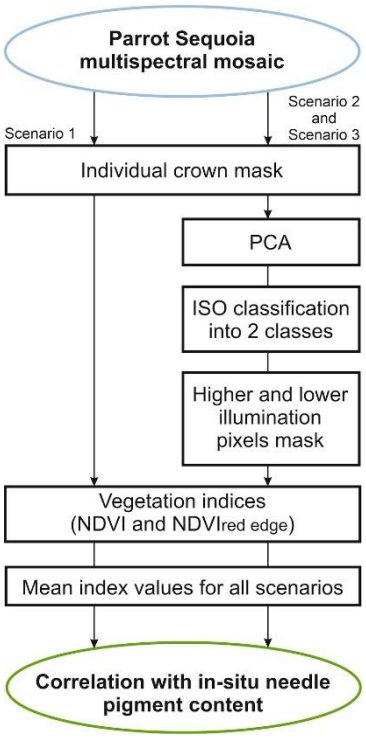

Figure 6. Parrot Sequoia multispectral data processing workflow chart.

2.6. Statistical evaluation

For Scenarios 1-3, the linear models between VIs (NDVI and $NDVI_{red\ edge}$) and ground truth (needle photosynthetic pigment contents defined in the laboratory) were derived individually. Since the extent to which the selection of the needle age as ground truth affects the model validity was tested, four ground truth age groups were created: i) all needles included, ii) 1st year needles included, iii) 2nd year needles included, and iv) 4 year old year needles included.

For the statistical evaluation of the linear models the coefficient of determination (R^2) was used:

$$R^2 = 1 - \frac{SS_{res}}{SS_{tot}}, \quad (4)$$

where SS_{res} represents the residual sum of squares and SS_{tot} represents total sum of squares [68].

3. Results

3.1. UAV photogrammetric products

The UAV data were acquired over 3 stands in the Lysina catchment (LYS 1K, LYS 2K, and LYS 4K) and 3 stands in the Pluhův Bor catchment (PLB 2K, PLB 3K, and PLB 5K). At each stand, the DSM, RGB and multispectral orthomosaics were created (Figure 7). The resulting spatial resolution and photogrammetric model errors are shown in Table 6. The total errors of the photogrammetric products oscillated around 1 m. The calculated vertical error of DSMs varied between 0.51 and 0.78 m. The obtained accuracy was considered sufficient for the purposes of this study. The RGB data from DJI Phantom 4 were then used mainly for a visual control while the calibrated multispectral data were used for further statistical assessment.

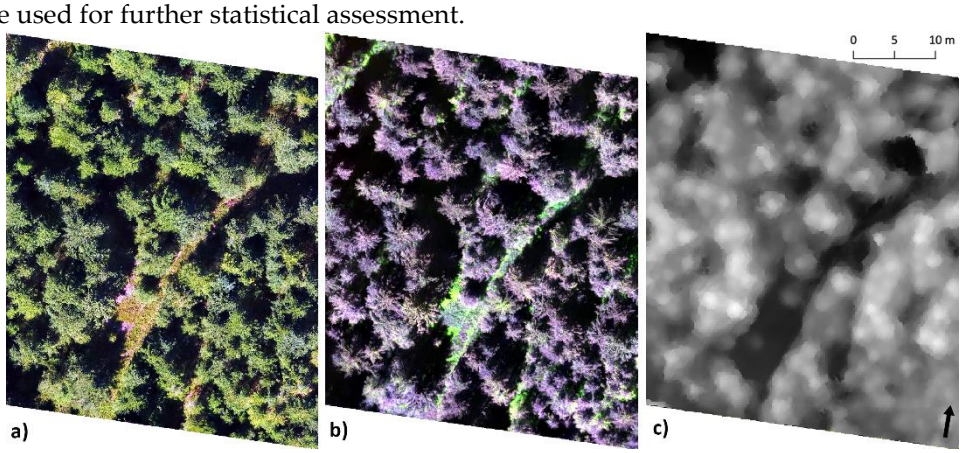

Preprints (www.preprints.org) | NOT PEER-REVIEWED | Posted: 13 January 2021 doi:10.20944/preprints202101.0255.v1

Figure 7. Example (LYS 2K) of the UAV survey products used in this study: (a) the RGB orthomosaic obtained from the DJI camera; (b) the multispectral mosaic derived from the Parrot Sequoia sensor (false-colour composition: Green, Red, Red edge); (c) the DSM derived from the Parrot Sequoia multispectral data.

Table 6. The resulting spatial resolution and photogrammetric model errors of multispectral and RGB data.

Test site	Parrot Sequoia - Multispectral Camera				DJI Camera - RGB	
	DSM (cm/px) *(Seq DSM)*	Orthomosaic (cm/px) *(Seq Mosaic)*	Vertical error (m)	Total error (m)	Orthomosaic (cm/px)	Total error (m)
LYS 1K	23.95	5.99	0.78	1.02	2.26	0.77
LYS 2K	16.41	4.09	0.55	0.67	1.12	1.14
LYS 4K	19.64	4.91	0.65	0.94	2.17	0.79
PLB 2K	23.30	5.82	0.51	0.82	2.05	0.71
PLB 3K	24.47	6.11	0.53	0.74	2.36	1.27
PLB 5K	23.00	5.74	0.61	0.72	1.87	0.83

3.2. UAV Tree height, crown and top detection

The tree characteristics - height, crown and top - derived from the CHM raster (Figure 8) were compared with the in-situ measurements collected in 2015 [45]. Table 7 summarizes the evaluation statistics. One stand - LYS 1K - showed very high error, for the other stands the success rate for the tree top identification varied between 72 and 87 %. (Table 7). When checking the in-situ data for LYS 1K, it was found that this stand is represented by significantly younger trees with the highest trees measured around 12 m. At this particular stand the trees were very dense and rather short, therefore tree detection could be problematic. As this stand also obtained very high errors in all other statistics, it was defined as an outlier and excluded from further statistics. In the case of tree crown estimation, the comparable success rate achieved varied between 76-94% (Table 7). In two cases, PLB 3K and PLB 5K, the tree crown detection results showed a higher number of estimated numbers than those measured in the field. This could possibly be caused by false crown splitting when using the tree shadow mask in the detection algorithm.

The box plots showing the distributions of tree height values for all stands - CHM-derived and in-situ - are displayed in Figure 9. Furthermore, following the assumption that the highest trees are the most recognizable by the detection algorithm, the results obtained for the 20 highest trees were assessed at each stand and their averaged CHM-estimated tree height values were compared with the in-situ data. It can be concluded that the tree height values derived for these trees from CHM were always higher than the in-situ measurements, the differences ranged between 1.54 - 2.36 m (Table 8). These differences are most probably a combination of the vertical error of the Seq DSM (0.51 - 0.78 m; Table 6) and tree growth between the years 2015 and 2018. However, the correlation between the estimated heights of the 20 tallest trees using CHM and in-situ measured data was high (Figure 10), as the coefficients of determination (R^2) obtained were higher than 0.90 in four out of five cases.

Preprints (www.preprints.org) | NOT PEER-REVIEWED | Posted: 13 January 2021 doi:10.20944/preprints202101.0255.v1

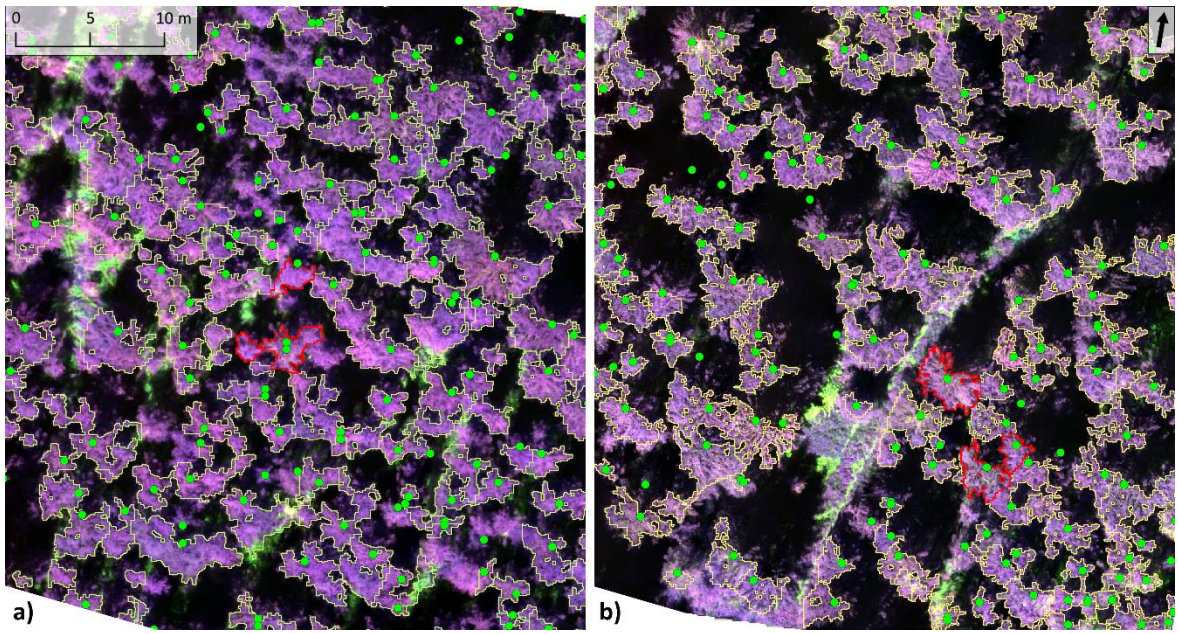

Figure 8. Example of result data from tree peak, height and crown detection process: (a) LYS 1K test location; (b) LYS 2K test location. Green dots represent estimated tree peaks, yellow polygons delineate detected tree crowns and red-line polygons show the three trees at each stand which were sampled for photosynthetic pigment contents. The background image is the Multispectral Parrot Sequoia mosaic (false-colour composition: Green, Red, Red edge).

Table 7. Comparison between the number of detected tree peaks and crowns (CHM-estimated) and in-situ measured data.

Test site	No. of trees measured in-situ (above set height mask)	No. of detected tree peaks based on UAV data	Success rate of detected tree tops (%) (compared to the trees measured in-situ)	No. of detected tree crowns based on UAV data	Success rate of detected tree crowns (%) (compared to the trees measured in-situ)
LYS 1K	177	45	25.42	61	34.46
LYS 2K	67	49	73.13	57	85.07
LYS 4K	25	18	72.00	19	76.00
PLB 2K	34	25	73.53	31	91.18
PLB 3K	15	13	86.66	17	86.67
PLB 5K	32	26	81.25	34	93.75

Preprints (www.preprints.org) | NOT PEER-REVIEWED | Posted: 13 January 2021 doi:10.20944/preprints202101.0255.v1

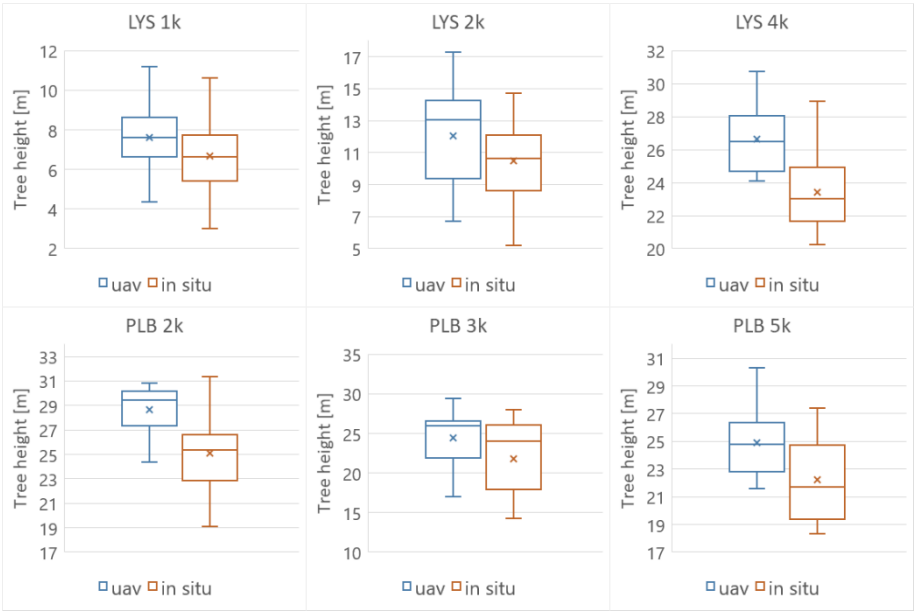

Figure 9. Tree height distribution visualized by box plots. Blue boxes represent trees detected by the automatic algorithm from UAV-based CHM data (2018) and orange boxes display the distribution of the tree heights measured in-situ in 2015.

Table 8. Comparison of average tree heights of the 20 tallest trees for each stand: CHM-estimated tree heights and the situ measured data.

Test site	Average tree top height (m) - in-situ data	Average tree top height (m) based on the CHM data	Difference of average tree heights (m)
LYS 2K	13.33	14.87	1.54
LYS 4K	24.34	26.62	2.28
PLB 2K	27.08	29.44	2.36
PLB 3K	22.86	24.63	1.77
PLB 5K	23.95	25.70	1.75

Preprints (www.preprints.org) | NOT PEER-REVIEWED | Posted: 13 January 2021 doi:10.20944/preprints202101.0255.v1

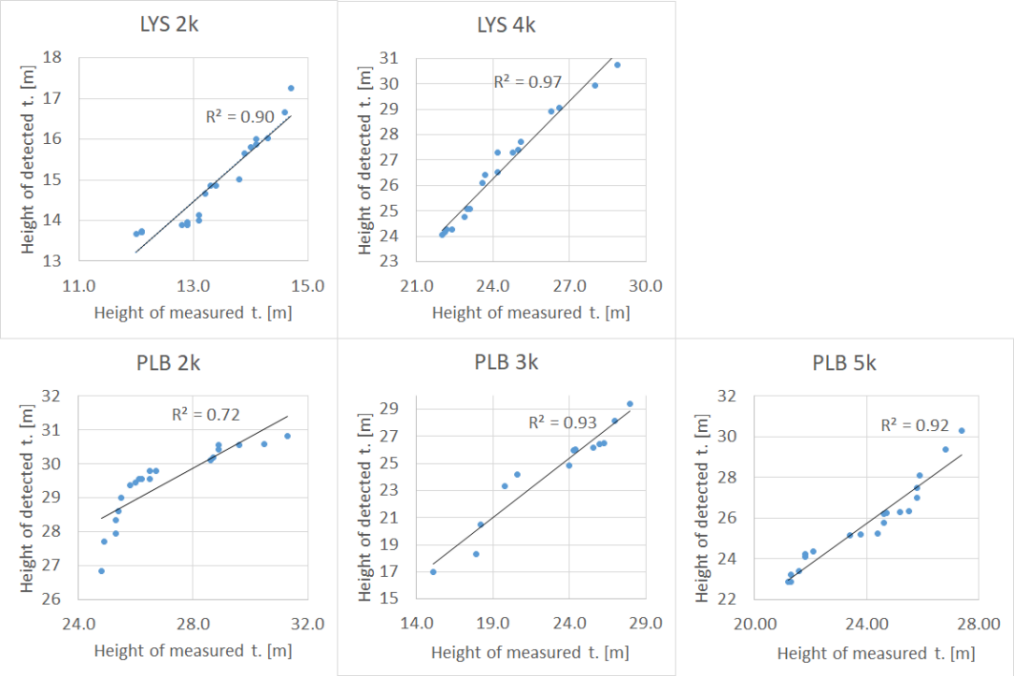

Figure 10. Linear regression and coefficients of determination (R^2): the CHM-estimated heights of the 20 highest trees at each stand compared to the in-situ data.

3.3. Relationship between selected vegetation indexes and the ground truth

Both tested catchment areas were characterized by comparable $NDVI_{red\ edge}$ values, however a bigger difference in the NDVI values could be seen between the LYS and PLB catchments (Table 9). In the methodological chapter (Section 2.5) three different scenarios were defined to assess the relationship between the spectral indices and photosynthetic pigments: Scenario 1: the whole crown (all pixels); Scenario 2: the top and the higher-illuminated part of the tree crown; Scenario 3: the lower-illuminated part of the tree crown. When comparing the results obtained for Scenarios 1-3 (Table 9, Figure 11) the NDVI index showed almost negligible differences among all three Scenarios, while the $NDVI_{red\ edge}$ index showed little bit bigger differences among the defined scenarios.

Table 9. Mean values of vegetation indices based on Sequoia optical data per evaluated Scenarios for both catchments.

	Catchment	Scenario 1	Scenario 2	Scenario 3
NDVI	Lysina (LYS)	0.836	0.832	0.829
	Pluhův Bor (PLB)	0.782	0.772	0.770
$NDVI_{red\ edge}$	Lysina (LYS)	0.138	0.130	0.149
	Pluhův Bor (PLB)	0.140	0.121	0.146

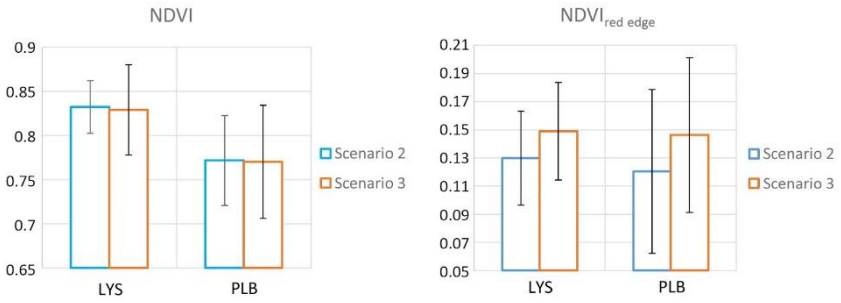

Preprints (www.preprints.org) | NOT PEER-REVIEWED | Posted: 13 January 2021 doi:10.20944/preprints202101.0255.v1

Figure 11. NDVI, $NDVI_{red\ edge}$: mean value and standard deviation for two illumination Scenarios 2 and 3 (summarized for each catchment area).

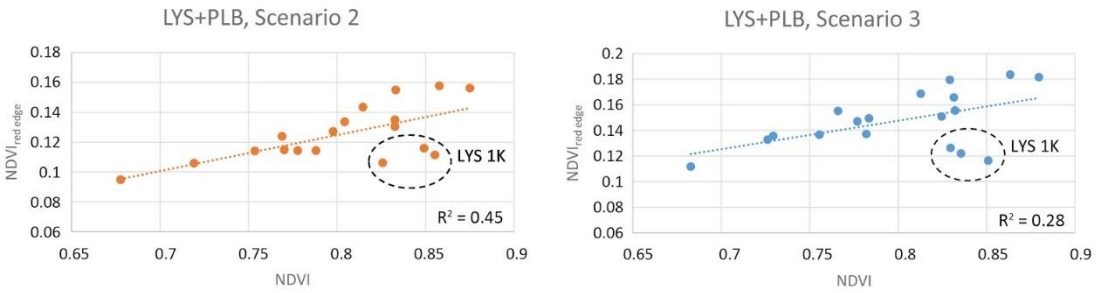

Figure 12. Linear regression of NDVI and $NDVI_{red\ edge}$ at evaluated catchments reaching R^2 values of 0.45 in Scenario 2 and 0.28 in Scenario 3. After excluding the LYS 1K stand, the R^2 values significantly increased (Scenario 2: $R^2 = 0.85$; Scenario 3: $R^2 = 0.84$).

Linear models were built between the VIs (NDVI and $NDVI_{red\ edge}$) and the ground truth (in-situ needle chlorophyll and carotenoid contents). As was mentioned in Section 3.2, the LYS 1K stand was identified as an outlier. Besides the significant difference in average tree age, which can be seen in Table 2, the LYS 1K stand was also identified as an outlier in the statistics derived for the VIs and was therefore excluded (Figure 12). As a result, there were 9 trees in total from the PLB catchment and 6 trees from the LYS catchment which were used for this statistical assessment. As already described, 3 different scenarios were used (Figure 14 and 15) for which the VIs were correlated with the ground truth (laboratory analysis of Chlorophyll a and b and carotenoids) using four different needle age groups too - all needles together included, 1st year needles included, 2nd year needles included and 4 year old needles included (Tables 10 and 11). For both VIs a similar pattern was identified. It can be concluded that the results differ significantly depending on what needle age group was used as ground truth. The worst results were obtained when the 1st year needle group was used (no correlation), followed by the 4 year old needle group and all age needle group used as ground truth (very weak correlation). On the other hand, for both VIs the best results were obtained when the 2nd year needle group was used as ground truth.

Assessing the different illumination crown conditions (Scenarios 1-3) in the case that the 2nd year needle group was selected as ground truth (Table 10-11, Figure 13-14), the worst results were surprisingly obtained for Scenario 2, where the top crown part receiving the higher-illumination was assessed, followed by Scenario 1 - the whole crown case; the best results were obtained for Scenario 3 - where the lower illumination part of the crown was assessed. For the NDVI index the differences between Scenarios 1 - 3 are very small, slightly bigger differences could be found for the $NDVI_{red\ edge}$ index. It can be concluded that the best results were achieved when the 2nd year needle group was used as ground truth together with Scenario 3 for both VIs. Using this setting for the NDVI index, the following R^2 were obtained for photosynthetic pigments (Table 10): Total chlorophyll - $R^2 = 0.49$, Chlorophyll a - $R^2 = 0.48$, Chlorophyll b - $R^2 = 0.51$ and Carotenoids - $R^2 = 0.50$. Comparable results were then also obtained for the $NDVI_{red\ edge}$ index (Table 11): Total chlorophyll - $R^2 = 0.46$, Chlorophyll a - $R^2 = 0.45$, Chlorophyll b - $R^2 = 0.48$ and Carotenoids - $R^2 = 0.52$. The NDVI index achieved a slightly higher R^2 for Total chlorophyll, Chlorophyll a and b contents while $NDVI_{red\ edge}$ showed slightly better results for Carotenoids.

Table 10. Coefficients of determination (R^2) for NDVI index and the four ground truth needle age groups.

NDVI	Parameter	Scenario 1	Scenario 2	Scenario 3

Preprints (www.preprints.org) | NOT PEER-REVIEWED | Posted: 13 January 2021 doi:10.20944/preprints202101.0255.v1

All needles	Total chlorophyll	0.33284	0.3132	0.34764
	Chlorophyll a	0.31794	0.30137	0.33012
	Chlorophyll b	0.36924	0.34138	0.39117
	Carotenoids	0.31854	0.2931	0.33969
1st year needles	Total chlorophyll	0.03731	0.04066	0.03605
	Chlorophyll a	0.03489	0.03854	0.03333
	Chlorophyll b	0.04373	0.04618	0.04336
	Carotenoids	0.07389	0.0579	0.08686
2nd year needles	Total chlorophyll	0.4801	0.44667	0.49043
	Chlorophyll A	0.47219	0.44141	0.48051
	Chlorophyll B	0.49659	0.45638	0.51224
	Carotenoids	0.48543	0.44873	0.50073
1st and 2nd year needles	Total chlorophyll	0.32343	0.30964	0.32722
	Chlorophyll a	0.31349	0.30185	0.31563
	Chlorophyll b	0.34721	0.32763	0.35556
	Carotenoids	0.34096	0.30585	0.36069
4+ years year needles	Total chlorophyll	0.21125	0.19238	0.23391
	Chlorophyll a	0.19768	0.18171	0.21753
	Chlorophyll b	0.24389	0.21744	0.27382
	Carotenoids	0.18607	0.16277	0.21334

Legend:

0.1>	0.1	0.2	0.3	0.4	0.5

Table 11. Coefficients of determination (R^2) for $NDVI_{red\ edge}$ index and the four ground truth age groups.

$NDVI_{red\ edge}$	Parameter	Scenario 1	Scenario 2	Scenario 3
All needles	Total chlorophyll	0.33424	0.3367	0.32031
	Chlorophyll a	0.32371	0.32902	0.30735
	Chlorophyll b	0.35841	0.35316	0.35132
	Carotenoids	0.37654	0.37009	0.36017
1st year needles	Total chlorophyll	0.03079	0.05179	0.01875
	Chlorophyll a	0.03029	0.05143	0.0181
	Chlorophyll b	0.03195	0.05241	0.0181
	Carotenoids	0.07625	0.09464	0.07331
2nd year needles	Total chlorophyll	0.44861	0.43218	0.46261
	Chlorophyll a	0.44209	0.42862	0.45333
	Chlorophyll b	0.46151	0.43743	0.48268
	Carotenoids	0.51865	0.50788	0.52091
1st and 2nd year needles	Total chlorophyll	0.29587	0.3163	0.28207
	Chlorophyll a	0.28979	0.31194	0.27428
	Chlorophyll b	0.3093	0.32489	0.30031
	Carotenoids	0.36182	0.37105	0.36049
4+ years year needles	Total chlorophyll	0.2499	0.22732	0.24152
	Chlorophyll a	0.23973	0.22026	0.22884
	Chlorophyll b	0.27252	0.24211	0.27104
	Carotenoids	0.26164	0.23661	0.25304

Legend:

0.1>	0.1	0.2	0.3	0.4	0.5

Preprints (www.preprints.org) | NOT PEER-REVIEWED | Posted: 13 January 2021 doi:10.20944/preprints202101.0255.v1

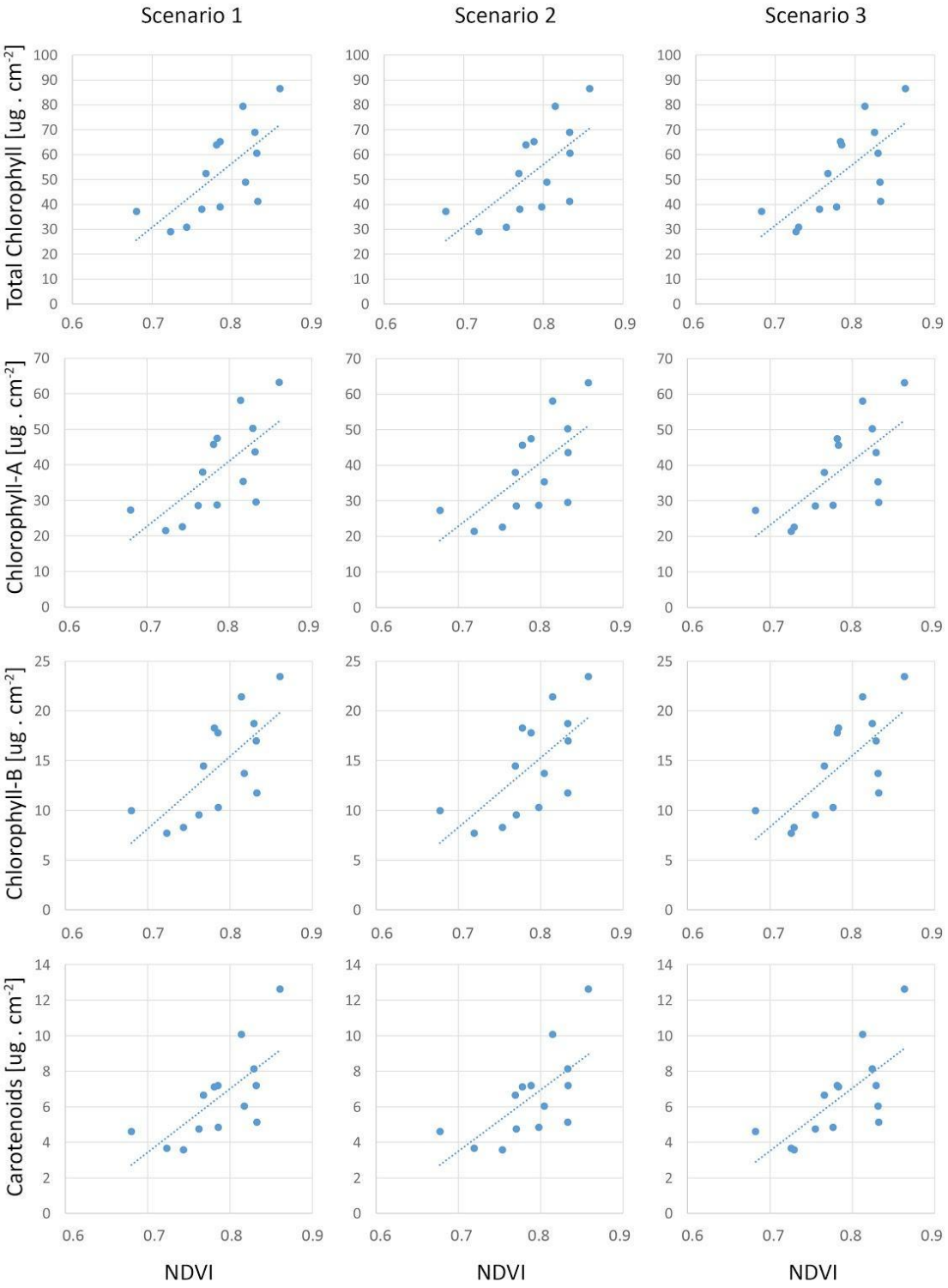

Figure 13. Linear regression between NDVI index and 2nd year needles photosynthetic pigment content for Scenarios 1-3.

Preprints (www.preprints.org) | NOT PEER-REVIEWED | Posted: 13 January 2021 doi:10.20944/preprints202101.0255.v1

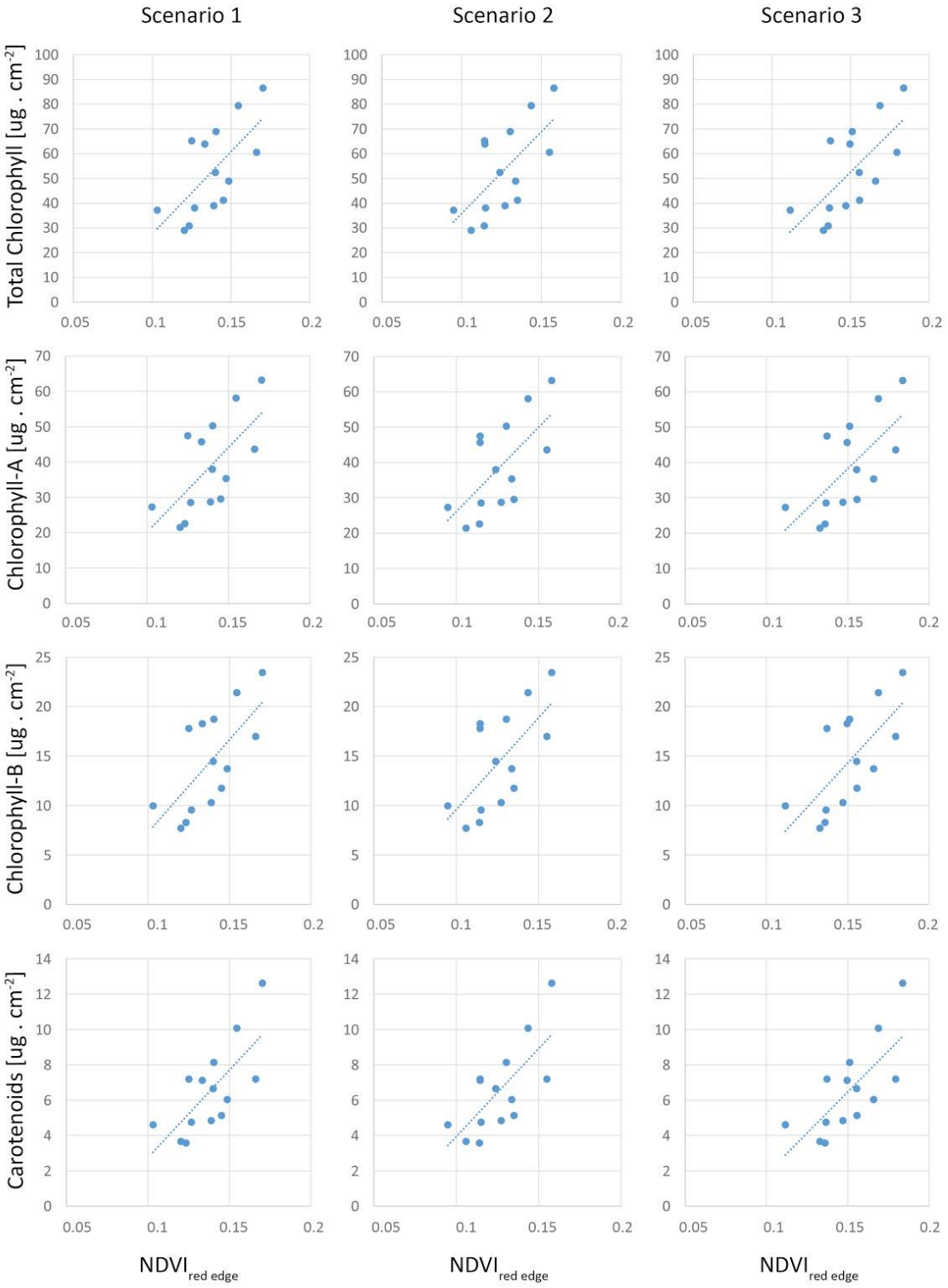

Figure 14. Linear regression between $NDVI_{red\ edge}$ index and 2nd year needles' photosynthetic pigment content for Scenarios 1-3.

4. Discussion

So far, most of the studies using UAVs and multispectral cameras have been carried out on agricultural species such as maize [69–71], sugar beet crops [72] and wheat [73,74]. As concerns woody species, the UAV-based approach has been applied to managed plantations with regular plant arrangement, such as vineyards [75] and fruit tree orchards [76,77]. Recently, the UAV-based

Preprints (www.preprints.org) | NOT PEER-REVIEWED | Posted: 13 January 2021 doi:10.20944/preprints202101.0255.v1

multispectral sensing has been used for high-throughput monitoring of photosynthetic activity in a white spruce (*Picea glauca*) seedling plantation [78]. When assessing the foliage traits of forest trees, it is necessary to take in account the tree size, branch geometry and foliage clumping. Dealing with evergreens, particularly conifers, a higher level of complexity emerges as different needle age generations contribute to the final signal received by the sensor. Few studies on forest health assessment using the UAVs and multispectral cameras have been published, Dash et al. [33] demonstrated the usefulness of such approaches for monitoring physiological stress in mature plantation trees even during the early stages of tree stress when using a non-parametric approach for the qualitative classification. Chianucci et al. [79] used the true colour images together with a fixed-wing UAV to quantify the canopy cover and leaf area index of beech forest stands. Dash et al. [80] tested the sensitivity of the multispectral image data time-series acquired by the UAV platform and satellite imagery to detect herbicide-induced stress in a controlled experiment conducted on a mature *Pinus radiata* plantation. Another successful qualitative forest health classification using UAVs and hyperspectral cameras has been demonstrated by Näsi et al. [35], and Berveglieri and Tommaselli [81]. It can be concluded that no study was found in which it was possible to directly compare the results of this study conducted on coniferous forest stands.

Regarding the first part of this analysis - tree height, crown and top detection - it can be concluded that the results obtained satisfy the requirements of this study, which is basically aimed at identifying individual tree crowns and masking the background and shades. A relatively quick method was employed using Seq DSM and high resolution DEM (DMR 5G) and it obtained reliable results achieving R^2=0.90 and higher between CHM-estimated heights and the in-situ tree measurements for most of the stands, with the exception of PLB 2K (R^2= 0.7) (Figure 10). The lower accuracy obtained for PLB 2K can be explained by changes happening between the time the in-situ data were collected (2015) and the UAV data acquisition (2018). In the field it was observed that tree cuts were common in this particular forest stand. It will be interesting to test in the future, if this approach can be further employed or adjusted for estimating the forest aboveground biomass in a similar way as airborne laser scanning has been employed [45].

Laboratory analyses of needles collected as a ground truth showed typical chlorophyll and carotenoid values (Table 3) for non-stressed mature Norway spruce trees in a similar region and at a similar altitude [46,82]. This was despite the fact that forest in the PLB catchment showed evidence of suppressed growth due to the nutritional stress caused by the extreme chemistry of the underlying bedrock [83]. This further indicated that photosynthetic pigment content alone provided a somewhat limited indication of stressed trees. At both study sites, almost all trees exhibited the usual accumulation of chlorophyll and carotenoids in older needles in comparison with the 1st year needles (Apendix A: Figure A1) [22,82,84]. Similarly as for needle biophysical traits, their optical properties are also influenced by needle age [85–87] in the following manner: for reflectance in Green and NIR (particularly 750-1000 nm) there is a decrease with needle age [46,86].

For both VIs a similar R^2 was obtained between the index values and the laboratory analysis of photosynthetic pigments, NDVI showed a slightly higher R^2 for chlorophyll content while $NDVI_{red\ edge}$ had the highest R^2 for carotenoid content. The Red edge is commonly used for detecting vegetation stress [88] and in this study it was also a slightly better index to estimate carotenoids - the vegetation stress indicators. The biggest influence on linear models for both was the selection of the needle age group used as a ground truth. As summarized in Tables 10 and 11, basically the only usable results were obtained when using the 2nd year needle pigment contents. The age-dependence of correlation strength between vegetation indices and measured pigment contents were expectable. However, the absence of a NDVI and $NDVI_{red\ edge}$ correlation to chlorophyll and carotenoids for the 1st year needles was highly surprising. Such needles were already fully developed at the date of sampling (August 4-5th), thus the immaturity of needles as a likely reason was excluded. Moreover, 1st year needles are routinely and successfully used for taking ground truth for a broad range of spectroscopic and remote sensing studies at various scales from leaf- to stand level [86,88–92].

However, in some studies, 2nd year needles, similarly as in this study, also proved to be the best option for predicting needle traits [46,93], although the physiological and optical causes have not

Preprints (www.preprints.org) | NOT PEER-REVIEWED | Posted: 13 January 2021 doi:10.20944/preprints202101.0255.v1

been elucidated. Second year needles were also successfully used as ground truth for pigment content estimation from multispectral UAV data in mature Scots spine (*Pinus sylvestris*) [92]. The authors justified the selection of the 2nd year needles literally as "avoiding non-representative outliers in current and mature needles" [92]. The absence of correlation between chlorophyll content in first year needles and vegetation indices could be partly related to other interfering needle traits than chlorophyll content itself. Although water has absorption features in near- and shortwave infrared region, it sometimes shows intercorrelation with chlorophyll content [94] and may influence its prediction from leaf spectral signal. The sampling year 2018 was rather dry and water content in needles exhibited the opposite (increasing) trend towards older needles in comparison to previous season 2017 (Apendix A: Figure A2). We hypothesize that lower water content in 1st year needles could also negatively influence chlorophyll prediction from NDVI and $NDVI_{red\ edge}$.

In addition, this study's results showed that 1st year needles exhibited the lowest chlorophyll contents (31-35 ug.cm^2, Table 3) and it can be hypothesized that such values, in combination with coniferous canopy structure, may be below the detection limit of the Parrot Sequoia multispectral camera. In a maize field case study [71] the authors concluded that hemispherical-conical reflectance factors, NDVI and chlorophyll red-edge index derived from the Sequoia sensor, exhibit bias for high and low reflective surfaces. In comparison to broadleaf trees, conifer canopy NIR reflectance is generally lower [95] due to needle clustering within shoots and self-shading [96,97] and it is speculated that the needle photosynthetic pigment contents of the 1st year needles were, in this case, too low to be resolved by the Parrot Sequoia multispectral camera, which has limited spectral resolution and sensitivity compared to hyperspectral sensors.

In this study, the crown light condition showed to be much less important than the needle age selection as a ground truth. Surprisingly the highest R^2 for both VIs were achieved when using the less sunlit, lower part of the crown (Scenario 3), followed by Scenario 1 (full crown) and then Scenario 2 (the more sun-lit top part of the crown). It seems that at such a high spatial resolution, achieved when using the UAV platform, the tree structure and the needle/branch position can cause these differences. As shown in Figure A3 (Apendix A), the tree branches of the more sun-lit top part of the crown have a different position; they are shorter and more pointed up, while the less sunlit lower part of the crown has wider and flatter branches thus the needles have a better position regarding the Sun, flight and sensor geometry. Also, the more sunlit top part of the crown is presented by a higher percentage of the 1st year needles, which were found to be problematic for the reasons discussed above. To date, the effect of heterogeneous light conditions within the crown on UAV-based leaf traits modelling was tested on broad leaved apple and pear trees with similar result to those in this study: the full canopy spectra provided, in some cases, more accurate models than only sunlit pixels [77]. The authors suggest that including the signal from the whole crown results in a bigger sample size which may lead to model improvement. However, it can be concluded that very little is known about this issue and a complex study on reflectance variations regarding the tree/crown structure, needle configuration and light conditions is still needed.

5. Conclusion

The results show that there is a big potential in using UAVs together with affordable multispectral cameras as a platform for monitoring forest status at a local scale, however, at high resolution. Tree crown delineation and derivation of other parameters such as tree top and height, which was based on the Canopy Height Model (CHM) obtained from two data sources - digital surface model derived from the Parrot Sequoia camera multispectral images (Seq DSM) and high resolution Digital Elevation Model (DEM: DMR 5G), corresponded well with the in-situ data and was satisfactory for the purposes of this study. The results of the conducted statistical analysis show that the two tested VIs (NDVI and $NDVI_{red\ edge}$) have a potential to assess photosynthetic pigments in Norway spruce forests at a semi-quantitative level, however the selection of needle-age as a ground truth was revealed to be a very important factor. The only usable results were obtained for linear models when using the 2nd year needle pigment contents as a ground truth.

Preprints (www.preprints.org) | NOT PEER-REVIEWED | Posted: 13 January 2021 doi:10.20944/preprints202101.0255.v1

On the other hand, the illumination conditions of the crown showed to have very little effect on the model's validity, whereas slightly better results were obtained when assessing the less sunlit lower part of the crown, which is characterized by wider and more flat branches. Compared to the whole crown Scenario, the improvement was very small and it is proposed that the whole part of the crown be used for simplicity. However, this effect might have a bigger impact on data with a very high spectral resolution (e.g. hyperspectral data) and further systematic research on reflectance variations regarding the tree/crown structure, needle configuration and light conditions is still needed. No study was found in which it was possible to directly compare these results conducted on coniferous (Norway spruce) forest stands, this shows that there is also a further need for studies dealing with a quantitative estimation of the biochemical variables of coniferous forests when employing spectral data acquired at the UAV platform at a very high spatial resolution.

Author Contributions: Conceptualization, V.K.-S.; methodology, V.K.-S..; software, L.K.; validation, F.O., Z.L. and Z.Z.; formal analysis, L.K., J.J., Z.L.; investigation, V.K.-S., F.O., Z L.,; resources, J.J., F.O., Z.L.; writing—original draft preparation, L.K., V.K.-S., Z.L., J.J., F.O; reviewing and editing of the first manuscript version, V.K.-S..; visualization, L.K., J.J.; supervision, V.K.-S..; project administration, V.K.-S.; All authors have read and agreed to the published version of the manuscript.

Funding: This research was funded by Czech Science Foundation (grant number 17-05743S) and Czech Geological Survey, grant no. 310360.

Acknowledgments: We thank to Miroslav Barták for helping us with the chlorophyll analyses.

Conflicts of Interest: The authors declare no conflict of interest.

Appendix A

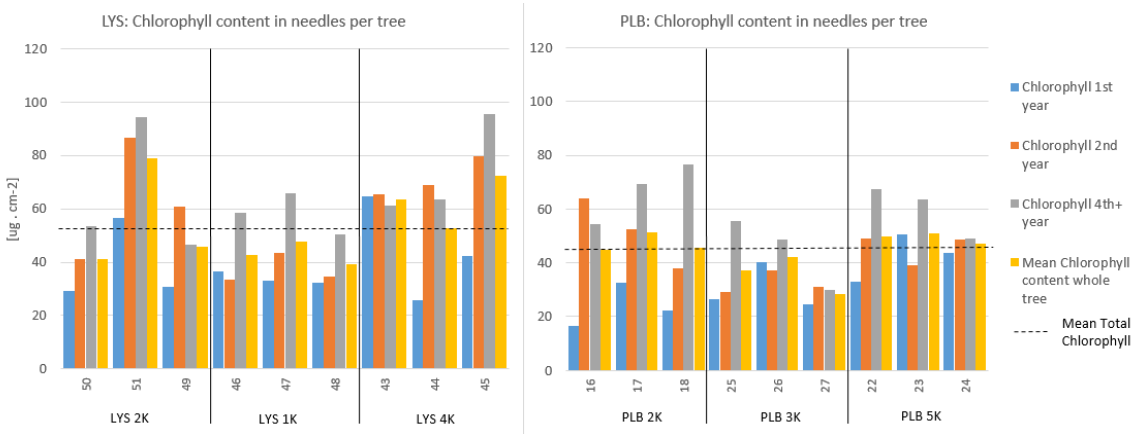

Figure A1. In-situ ground truth - biochemically assessed total chlorophyll content in different needle age classes of studied trees. In most cases chlorophyll content increased from 1st to 2nd year needles and usually the pigment further accumulated in older needles.

Preprints (www.preprints.org) | NOT PEER-REVIEWED | Posted: 13 January 2021 doi:10.20944/preprints202101.0255.v1

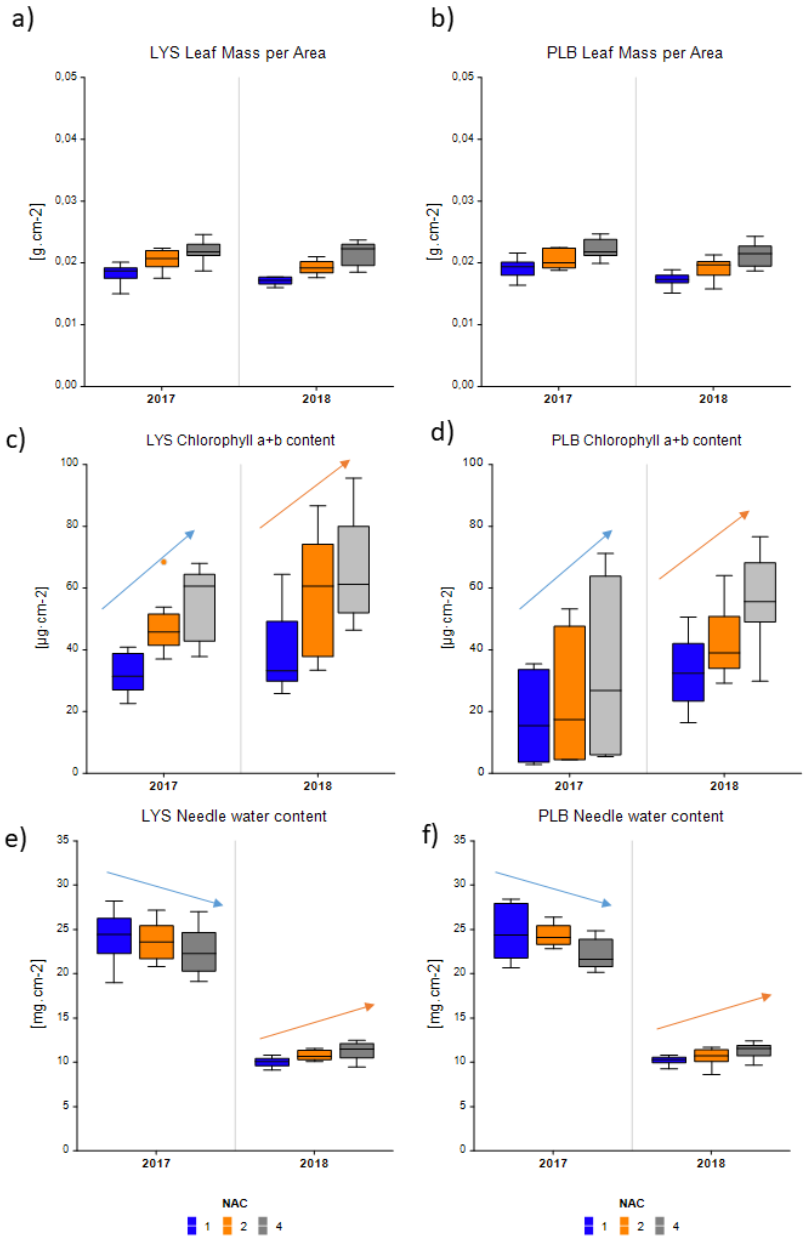

Figure A2. Selected biophysical traits of needles at LYS and PLB sites in 2017 (year before sampling) and 2018 (year of sampling and UAV data acquisition). (a), (b) Leaf mass per area; (c), (d) Needle chlorophyll content; (e), (f) Needle water content per area basis. NAC = needle age class: 1 – first year needles, 2 – second year needles, 4 – four years and older needles.

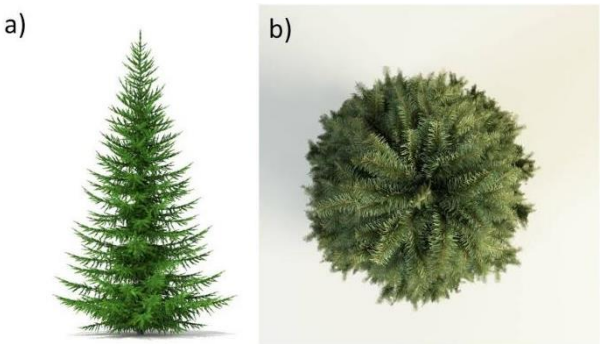

Figure A3. 3D representation of a solitary growing coniferous tree with a Norway spruce-like crown architecture. Side (a) and nadir view (b).

References

1. Potapov, P.; Yaroshenko, A.; Turubanova, S.; Dubinin, M.; Laestadius, L.; Thies, C.; Aksenov, D.; Egorov, A.; Yesipova, Y.; Glushkov, I. Mapping the World's Intact Forest Landscapes by Remote Sensing. *Ecol. Soc.* **2008**, *13*.
2. Boyd, D.S.; Danson, F.M. Satellite Remote Sensing of Forest Resources: Three Decades of Research Development. *Prog. Phys. Geogr.* **2005**, *29*, 1–26.
3. De Vries, W.; Vel, E.; Reinds, G.J.; Deelstra, H.; Klap, J.M.; Leeters, E.; Hendriks, C.M.A.; Kerkvoorden, M.; Landmann, G.; Herkendell, J. Intensive Monitoring of Forest Ecosystems in Europe: 1. Objectives, Set-up and Evaluation Strategy. *For. Ecol. Manag.* **2003**, *174*, 77–95.
4. Pause, M.; Schweitzer, C.; Rosenthal, M. *In Situ/Remote Sensing Integration to Assess Forest Health—a Review. Remote Sens*; 2016;
5. Žibret, G.; Kopačková, V. Comparison of Two Methods for Indirect Measurement of Atmospheric Dust Deposition: Street-Dust Composition and Vegetation-Health Status Derived from Hyperspectral Image Data. *Ambio* **2019**, *48*, 423–435, doi:10.1007/s13280-018-1093-0.
6. Hruška, J.; Krám, P. Modelling Long-Term Changes in Stream Water and Soil Chemistry in Catchments with Contrasting Vulnerability to Acidification (Lysina and Pluhuv Bor, Czech Republic). *Hydrol. Earth Syst. Sci.* **2003**, *7*, 525–539.
7. Švik, M.; Oulehle, F.; Krám, P.; Janoutová, R.; Tajovská, K.; Homolová, L. Landsat-Based Indices Reveal Consistent Recovery of Forested Stream Catchments from Acid Deposition. *Remote Sens.* **2020**, *12*, 1944.
8. Fottová, D.; Skořepová, I. Changes in mass element fluxes and their importance for critical loads: GEOMON network, Czech Republic. In *Biogeochemical Investigations at Watershed, Landscape, and Regional Scales*; Springer, 1998; pp. 365–376.
9. Fottová, D. Trends in Sulphur and Nitrogen Deposition Fluxes in the GEOMON Network, Czech Republic, between 1994 and 2000. *Water. Air. Soil Pollut.* **2003**, *150*, 73–87.
10. Oulehle, F.; Chuman, T.; Hruška, J.; Krám, P.; McDowell, W.H.; Myška, O.; Navrátil, T.; Tesař, M. Recovery from Acidification Alters Concentrations and Fluxes of Solutes from Czech Catchments. *Biogeochemistry* **2017**, *132*, 251–272.
11. Krám, P.; Hruška, J.; Shanley, J.B. Streamwater Chemistry in Three Contrasting Monolithologic Czech Catchments. *Appl. Geochem.* **2012**, *27*, 1854–1863.
12. Navrátil, T.; Kurz, D.; Krám, P.; Hofmeister, J.; Hruška, J. Acidification and Recovery of Soil at a Heavily Impacted Forest Catchment (Lysina, Czech Republic)—SAFE Modeling and Field Results. *Ecol. Model.* **2007**, *205*, 464–474.
13. Oulehle, F.; McDowell, W.H.; Aitkenhead-Peterson, J.A.; Krám, P.; Hruška, J.; Navrátil, T.; Buzek, F.; Fottová, D. Long-Term Trends in Stream Nitrate Concentrations and Losses across Watersheds Undergoing Recovery from Acidification in the Czech Republic. *Ecosystems* **2008**, *11*, 410–425.
14. Santos, A.A. dos; Marcato Junior, J.; Araújo, M.S.; Di Martini, D.R.; Tetila, E.C.; Siqueira, H.L.; Aoki, C.; Eltner, A.; Matsubara, E.T.; Pistori, H. Assessment of CNN-Based Methods for Individual Tree Detection on Images Captured by RGB Cameras Attached to UAVs. *Sensors* **2019**, *19*, 3595.
15. Fujimoto, A.; Haga, C.; Matsui, T.; Machimura, T.; Hayashi, K.; Sugita, S.; Takagi, H. An End to End Process Development for UAV-SfM Based Forest Monitoring: Individual Tree Detection, Species Classification and Carbon Dynamics Simulation. *Forests* **2019**, *10*, 680.
16. Fayad, I.; Baghdadi, N.; Guitet, S.; Bailly, J.-S.; Hérault, B.; Gond, V.; El Hajj, M.; Minh, D.H.T. Aboveground Biomass Mapping in French Guiana by Combining Remote Sensing, Forest Inventories and Environmental Data. *Int. J. Appl. Earth Obs. Geoinformation* **2016**, *52*, 502–514.
17. White, J.C.; Coops, N.C.; Wulder, M.A.; Vastaranta, M.; Hilker, T.; Tompalski, P. Remote Sensing Technologies for Enhancing Forest Inventories: A Review. *Can. J. Remote Sens.* **2016**, *42*, 619–641.
18. Masek, J.G.; Hayes, D.J.; Hughes, M.J.; Healey, S.P.; Turner, D.P. The Role of Remote Sensing in Process-Scaling Studies of Managed Forest Ecosystems. *For. Ecol. Manag.* **2015**, *355*, 109–123.
19. Lausch, A.; Heurich, M.; Gordalla, D.; Dobner, H.-J.; Gwillym-Margianto, S.; Salbach, C. Forecasting Potential Bark Beetle Outbreaks Based on Spruce Forest Vitality Using Hyperspectral Remote-Sensing Techniques at Different Scales. *For. Ecol. Manag.* **2013**, *308*, 76–89.
20. Halme, E.; Pellikka, P.; Mõttus, M. Utility of Hyperspectral Compared to Multispectral Remote Sensing Data in Estimating Forest Biomass and Structure Variables in Finnish Boreal Forest. *Int. J. Appl. Earth Obs. Geoinformation* **2019**, *83*, 101942.

21. Jarocińska, A.; Białczak, M.; Sławik, Ł. Application of Aerial Hyperspectral Images in Monitoring Tree Biophysical Parameters in Urban Areas. *Misc. Geogr.* **2018**, *22*, 56–62, doi:10.1515/mgrsd-2017-0034.
22. Kopačková, V.; Mišurec, J.; Lhotáková, Z.; Oulehle, F.; Albrechtová, J. Using Multi-Date High Spectral Resolution Data to Assess the Physiological Status of Macroscopically Undamaged Foliage on a Regional Scale. *Int. J. Appl. Earth Obs. Geoinformation* **2014**, *27*, 169–186, doi:10.1016/j.jag.2013.09.009.
23. Machala, M.; Zejdová, L. Forest Mapping Through Object-Based Image Analysis of Multispectral and LiDAR Aerial Data. *Eur. J. Remote Sens.* **2014**, *47*, 117–131, doi:10.5721/EuJRS20144708.
24. Mišurec, J.; Kopačková, V.; Lhotáková, Z.; Campbell, P.; Albrechtová, J. Detection of Spatio-Temporal Changes of Norway Spruce Forest Stands in Ore Mountains Using Landsat Time Series and Airborne Hyperspectral Imagery. *Remote Sens.* **2016**, *8*, 92, doi:10.3390/rs8020092.
25. Lin, Y.; Jiang, M.; Yao, Y.; Zhang, L.; Lin, J. Use of UAV Oblique Imaging for the Detection of Individual Trees in Residential Environments. *Urban For. Urban Green.* **2015**, *14*, 404–412, doi:10.1016/j.ufug.2015.03.003.
26. Klein Hentz, Â.M.; Corte, A.P.D.; Péllico Netto, S.; Strager, M.P.; Schoeninger, E.R. Treedetection: Automatic Tree Detection Using UAV-Based Data. *FLORESTA* **2018**, *48*, 393, doi:10.5380/rf.v48i3.56150.
27. Candiago, S.; Remondino, F.; De Giglio, M.; Dubbini, M.; Gattelli, M. Evaluating Multispectral Images and Vegetation Indices for Precision Farming Applications from UAV Images. *Remote Sens.* **2015**, *7*, 4026–4047, doi:10.3390/rs70404026.
28. Sona, G.; Passoni, D.; Pinto, L.; Pagliari, D.; Masseroni, D.; Ortuani, B.; Facchi, A. UAV Multispectral Survey to Map Soil and Crop for Precision Farming Applications. *ISPRS - Int. Arch. Photogramm. Remote Sens. Spat. Inf. Sci.* **2016**, *XLI-B1*, 1023–1029, doi:10.5194/isprsarchives-XLI-B1-1023-2016.
29. Albetis, J.; Duthoit, S.; Guttler, F.; Jacquin, A.; Goulard, M.; Poilvé, H.; Féret, J.-B.; Dedieu, G. Detection of Flavescence Dorée Grapevine Disease Using Unmanned Aerial Vehicle (UAV) Multispectral Imagery. *Remote Sens.* **2017**, *9*, 308, doi:10.3390/rs9040308.
30. Su, J.; Liu, C.; Hu, X.; Xu, X.; Guo, L.; Chen, W.-H. Spatio-Temporal Monitoring of Wheat Yellow Rust Using UAV Multispectral Imagery. *Comput. Electron. Agric.* **2019**, *167*, 105035, doi:10.1016/j.compag.2019.105035.
31. Baluja, J.; Diago, M.P.; Balda, P.; Zorer, R.; Meggio, F.; Morales, F.; Tardaguila, J. Assessment of Vineyard Water Status Variability by Thermal and Multispectral Imagery Using an Unmanned Aerial Vehicle (UAV). *Irrig. Sci.* **2012**, *30*, 511–522, doi:10.1007/s00271-012-0382-9.
32. Turner, D.; Lucieer, A.; Watson, C. Development of an Unmanned Aerial Vehicle (UAV) for Hyper Resolution Vineyard Mapping Based on Visible, Multispectral, and Thermal Imagery. In Proceedings of the Proceedings of 34th International Symposium on Remote Sensing of Environment; Sydney, Australia, April 10 2011; p. 4.
33. Dash, J.P.; Watt, M.S.; Pearse, G.D.; Heaphy, M.; Dungey, H.S. Assessing Very High Resolution UAV Imagery for Monitoring Forest Health during a Simulated Disease Outbreak. *ISPRS J. Photogramm. Remote Sens.* **2017**, *131*, 1–14, doi:10.1016/j.isprsjprs.2017.07.007.
34. Minařík, R.; Langhammer, J. Use of a Multispectral UAV Photogrammetry for Detection and Tracking of Forest Disturbance Dynamics. *ISPRS - Int. Arch. Photogramm. Remote Sens. Spat. Inf. Sci.* **2016**, *XLI-B8*, 711–718, doi:10.5194/isprsarchives-XLI-B8-711-2016.
35. Näsi, R.; Honkavaara, E.; Lyytikäinen-Saarenmaa, P.; Blomqvist, M.; Litkey, P.; Hakala, T.; Viljanen, N.; Kantola, T.; Tanhuanpää, T.; Holopainen, M. Using UAV-Based Photogrammetry and Hyperspectral Imaging for Mapping Bark Beetle Damage at Tree-Level. *Remote Sens.* **2015**, *7*, 15467–15493, doi:10.3390/rs71115467.
36. Franklin, S.E. Pixel- and Object-Based Multispectral Classification of Forest Tree Species from Small Unmanned Aerial Vehicles. *J. Unmanned Veh. Syst.* **2018**, *6*, 195–211, doi:10.1139/juvs-2017-0022.
37. Lim, Y.S.; La, P.H.; Park, J.S.; Lee, M.H.; Pyeon, M.W.; Kim, J.-I. Calculation of Tree Height and Canopy Crown from Drone Images Using Segmentation. 한국측량학회지 **2015**, *33*, 605–614, doi:10.7848/KSGPC.2015.33.6.605.
38. Díaz-Varela, R.; de la Rosa, R.; León, L.; Zarco-Tejada, P. High-Resolution Airborne UAV Imagery to Assess Olive Tree Crown Parameters Using 3D Photo Reconstruction: Application in Breeding Trials. *Remote Sens.* **2015**, *7*, 4213–4232, doi:10.3390/rs70404213.

39. Wu, X.; Shen, X.; Cao, L.; Wang, G.; Cao, F. Assessment of Individual Tree Detection and Canopy Cover Estimation Using Unmanned Aerial Vehicle Based Light Detection and Ranging (UAV-LiDAR) Data in Planted Forests. *Remote Sens.* **2019**, *11*, 908, doi:10.3390/rs11080908.
40. Panagiotidis, D.; Abdollahnejad, A.; Surový, P.; Chiteculo, V. Determining Tree Height and Crown Diameter from High-Resolution UAV Imagery. *Int. J. Remote Sens.* **2017**, *38*, 2392–2410, doi:10.1080/01431161.2016.1264028.
41. Jaakkola, A.; Hyyppä, J.; Yu, X.; Kukko, A.; Kaartinen, H.; Liang, X.; Hyyppä, H.; Wang, Y. Autonomous Collection of Forest Field Reference—The Outlook and a First Step with UAV Laser Scanning. *Remote Sens.* **2017**, *9*, 785, doi:10.3390/rs9080785.
42. Zaforemska, A.; Xiao, W.; Gaulton, R. Individual Tree Detection from UAV LIDAR Data in a Mixed Species Woodland. *ISPRS - Int. Arch. Photogramm. Remote Sens. Spat. Inf. Sci.* **2019**, *XLII-2/W13*, 657–663, doi:10.5194/isprs-archives-XLII-2-W13-657-2019.
43. Li, J.; Yang, B.; Cong, Y.; Cao, L.; Fu, X.; Dong, Z. 3D Forest Mapping Using A Low-Cost UAV Laser Scanning System: Investigation and Comparison. *Remote Sens.* **2019**, *11*, 717, doi:10.3390/rs11060717.
44. ČÚZK: Geoportál Available online: https://geoportal.cuzk.cz/(S(5rmwjwtpueumnrsepeeaarwk))/Default.aspx?head_tab=sekce-00-gp&mode=TextMeta&text=uvod_uvod&menu=01&news=yes&UvodniStrana=yes (accessed on 31 December 2020).
45. Novotný, J.; Navrátilová, B.; Janoutová, R.; Oulehle, F.; Homolová, L. Influence of Site-Specific Conditions on Estimation of Forest above Ground Biomass from Airborne Laser Scanning. *Forests* **2020**, *11*, 268, doi:10.3390/f11030268.
46. Lhotáková, Z.; Kopačková-Strnadová, V.; Oulehle, F.; Homolová, L.; Neuwirthová, E.; Švik, M.; Janoutová, R.; Albrechtová, J. Foliage Biophysical Trait Prediction from Laboratory Spectra in Norway Spruce Is More Affected by Needle Age than by Site Soil Conditions. *Remote Sens.* (under review).
47. Porra, R.J.; Thompson, W.A.; Kriedemann, P.E. Determination of Accurate Extinction Coefficients and Simultaneous Equations for Assaying Chlorophylls a and b Extracted with Four Different Solvents: Verification of the Concentration of Chlorophyll Standards by Atomic Absorption Spectroscopy. *Biochim. Biophys. Acta BBA - Bioenerg.* **1989**, *975*, 384–394, doi:10.1016/S0005-2728(89)80347-0.
48. Wellburn, A.R. The Spectral Determination of Chlorophylls a and b, as Well as Total Carotenoids, Using Various Solvents with Spectrophotometers of Different Resolution. *J. Plant Physiol.* **1994**, *144*, 307–313, doi:10.1016/S0176-1617(11)81192-2.
49. DJI - Official Website Available online: https://www.dji.com (accessed on 30 December 2020).
50. Phantom 4 - DJI Available online: https://www.dji.com/phantom-4 (accessed on 30 December 2020).
51. SenseFly - SenseFly – The Professional's Mapping Drone Available online: https://www.sensefly.com/ (accessed on 30 December 2020).
52. Prusa3D - Open-Source 3D Printers from Josef Prusa Available online: https://www.prusa3d.com/ (accessed on 30 December 2020).
53. Litchi for DJI Mavic / Phantom / Inspire / Spark Available online: https://flylitchi.com/ (accessed on 31 December 2020).
54. Best Practices: Collecting Data with MicaSense Sensors Available online: https://support.micasense.com/hc/en-us/articles/224893167-Best-practices-Collecting-Data-with-MicaSense-Sensors (accessed on 31 December 2020).
55. Agisoft Metashape Available online: https://www.agisoft.com/ (accessed on 31 December 2020).
56. Westoby, M.J.; Brasington, J.; Glasser, N.F.; Hambrey, M.; Reynolds, J.M. 'Structure-from-Motion' Photogrammetry: A Low-Cost, Effective Tool for Geoscience Applications. *Geomorphology* **2012**, *179*, 300–314, doi:10.1016/j.geomorph.2012.08.021.
57. Tutorial (Intermediate Level):Radiometric Calibration Using Reflectance Panelsin PhotoScan Professional 1.4 Available online: https://www.agisoft.com/pdf/PS_1.4_(IL)_Refelctance_Calibration.pdf (accessed on 20 December 2020).
58. Zhao, K.; Popescu, S. Hierarchical Watershed Segmentation of Canopy Height Model for Multi-Scale Forest Inventory. In Proceedings of the Proceedings of the ISPRS working group "Laser Scanning 2007 and SilviLaser 2007"; Espoo, Finland, September 12 2007; pp. 436–440.
59. Hubacek, M.; Kovarik, V.; Kratochvil, V. Analysis of Influence of Terrain Relief Roughness on DEM Accuracy Generated from LIDAR in the Czech Republic Territory. In Proceedings of the ISPRS - International Archives of the Photogrammetry, Remote Sensing and Spatial Information Sciences; Copernicus GmbH, June 10 2016; Vol. XLI-B4, pp. 25–30.

60. How Focal Statistics Works—Help | ArcGIS for Desktop Available online: https://desktop.arcgis.com/en/arcmap/10.3/tools/spatial-analyst-toolbox/how-focal-statistics-works.htm (accessed on 31 December 2020).
61. Xu, N.; Tian, J.; Tian, Q.; Xu, K.; Tang, S. Analysis of Vegetation Red Edge with Different Illuminated/Shaded Canopy Proportions and to Construct Normalized Difference Canopy Shadow Index. *Remote Sens.* **2019**, *11*, 1192, doi:10.3390/rs11101192.
62. Rouse, J.W.; Hass, R.H.; Schell, J.A.; Deering, D.W.; Harlan, J.C. *Monitoring the Vernal Advancement and Retrogradation (Green Wave Effect) of Natural Vegetation.*; RSC 1978-4; Texas A & M University: College Station, Texas, 1974;
63. Sharma, L.; Bu, H.; Denton, A.; Franzen, D. Active-Optical Sensors Using Red NDVI Compared to Red Edge NDVI for Prediction of Corn Grain Yield in North Dakota, U.S.A. *Sensors* **2015**, *15*, 27832–27853, doi:10.3390/s151127832.
64. Gitelson, A.; Merzlyak, M.N. Spectral Reflectance Changes Associated with Autumn Senescence of Aesculus Hippocastanum L. and Acer Platanoides L. Leaves. Spectral Features and Relation to Chlorophyll Estimation. *J. Plant Physiol.* **1994**, *143*, 286–292, doi:10.1016/S0176-1617(11)81633-0.
65. Sims, D.A.; Gamon, J.A. Relationships between Leaf Pigment Content and Spectral Reflectance across a Wide Range of Species, Leaf Structures and Developmental Stages. *Remote Sens. Environ.* **2002**, *81*, 337–354, doi:10.1016/S0034-4257(02)00010-X.
66. Chavez Jr., P.S.; Kwarteng, A.Y. Extracting Spectral Contrast in Landsat Thematic Mapper Image Data Using Selective Principal Component Analysis. *Photogramm. Eng. Remote Sens.* **1989**, *55*, 10.
67. Mather, P.M.; Koch, M. *Computer Processing of Remotely-Sensed Images: An Introduction*; 4th ed.; Wiley-Blackwell: Chichester, West Sussex, UK ; Hoboken, NJ, 2011; ISBN 978-0-470-74239-6.
68. Draper, N.R.; Smith, H. *Applied Regression Analysis*; Wiley Series in Probability and Statistics; 1st ed.; Wiley, 1998; ISBN 978-0-471-17082-2.
69. Singhal, G.; Bansod, B.; Mathew, L.; Goswami, J.; Choudhury, B.U.; Raju, P.L.N. Chlorophyll Estimation Using Multi-Spectral Unmanned Aerial System Based on Machine Learning Techniques. *Remote Sens. Appl. Soc. Environ.* **2019**, *15*, 100235, doi:10.1016/j.rsase.2019.100235.
70. Guo, Y.; Wang, H.; Wu, Z.; Wang, S.; Sun, H.; Senthilnath, J.; Wang, J.; Robin Bryant, C.; Fu, Y. Modified Red Blue Vegetation Index for Chlorophyll Estimation and Yield Prediction of Maize from Visible Images Captured by UAV. *Sensors* **2020**, *20*, 5055, doi:10.3390/s20185055.
71. Fawcett, D.; Panigada, C.; Tagliabue, G.; Boschetti, M.; Celesti, M.; Evdokimov, A.; Biriukova, K.; Colombo, R.; Miglietta, F.; Rascher, U.; et al. Multi-Scale Evaluation of Drone-Based Multispectral Surface Reflectance and Vegetation Indices in Operational Conditions. *Remote Sens.* **2020**, *12*, 514, doi:10.3390/rs12030514.
72. Jay, S.; Baret, F.; Dutartre, D.; Malatesta, G.; Héno, S.; Comar, A.; Weiss, M.; Maupas, F. Exploiting the Centimeter Resolution of UAV Multispectral Imagery to Improve Remote-Sensing Estimates of Canopy Structure and Biochemistry in Sugar Beet Crops. *Remote Sens. Environ.* **2019**, *231*, 110898, doi:10.1016/j.rse.2018.09.011.
73. Hassan, M.; Yang, M.; Rasheed, A.; Jin, X.; Xia, X.; Xiao, Y.; He, Z. Time-Series Multispectral Indices from Unmanned Aerial Vehicle Imagery Reveal Senescence Rate in Bread Wheat. *Remote Sens.* **2018**, *10*, 809, doi:10.3390/rs10060809.
74. Lu, N.; Wang, W.; Zhang, Q.; Li, D.; Yao, X.; Tian, Y.; Zhu, Y.; Cao, W.; Baret, F.; Liu, S.; et al. Estimation of Nitrogen Nutrition Status in Winter Wheat From Unmanned Aerial Vehicle Based Multi-Angular Multispectral Imagery. *Front. Plant Sci.* **2019**, *10*, 1601, doi:10.3389/fpls.2019.01601.
75. Zarco-Tejada, P.J.; Guillén-Climent, M.L.; Hernández-Clemente, R.; Catalina, A.; González, M.R.; Martín, P. Estimating Leaf Carotenoid Content in Vineyards Using High Resolution Hyperspectral Imagery Acquired from an Unmanned Aerial Vehicle (UAV). *Agric. For. Meteorol.* **2013**, *171–172*, 281–294, doi:10.1016/j.agrformet.2012.12.013.
76. Berni, J.; Zarco-Tejada, P.J.; Suarez, L.; Fereres, E. Thermal and Narrowband Multispectral Remote Sensing for Vegetation Monitoring From an Unmanned Aerial Vehicle. *IEEE Trans. Geosci. Remote Sens.* **2009**, *47*, 722–738, doi:10.1109/TGRS.2008.2010457.
77. Vanbrabant, Y.; Tits, L.; Delalieux, S.; Pauly, K.; Verjans, W.; Somers, B. Multitemporal Chlorophyll Mapping in Pome Fruit Orchards from Remotely Piloted Aircraft Systems. *Remote Sens.* **2019**, *11*, 1468, doi:10.3390/rs11121468.

78. D'Odorico, P.; Besik, A.; Wong, C.Y.S.; Isabel, N.; Ensminger, I. High-throughput Drone-based Remote Sensing Reliably Tracks Phenology in Thousands of Conifer Seedlings. *New Phytol.* **2020**, *226*, 1667–1681, doi:10.1111/nph.16488.
79. Chianucci, F.; Disperati, L.; Guzzi, D.; Bianchini, D.; Nardino, V.; Lastri, C.; Rindinella, A.; Corona, P. Estimation of Canopy Attributes in Beech Forests Using True Colour Digital Images from a Small Fixed-Wing UAV. *Int. J. Appl. Earth Obs. Geoinformation* **2016**, *47*, 60–68, doi:10.1016/j.jag.2015.12.005.
80. Dash, J.; Pearse, G.; Watt, M. UAV Multispectral Imagery Can Complement Satellite Data for Monitoring Forest Health. *Remote Sens.* **2018**, *10*, 1216, doi:10.3390/rs10081216.
81. Berveglieri, A.; Tommaselli, A.M.G. Exterior Orientation of Hyperspectral Frame Images Collected with UAV for Forest Applications. *ISPRS - Int. Arch. Photogramm. Remote Sens. Spat. Inf. Sci.* **2016**, *XL-3/W4*, 45–50, doi:10.5194/isprsarchives-XL-3-W4-45-2016.
82. Homolová, L.; Lukeš, P.; Malenovský, Z.; Lhotáková, Z.; Kaplan, V.; Hanuš, J. Measurement Methods and Variability Assessment of the Norway Spruce Total Leaf Area: Implications for Remote Sensing. *Trees* **2013**, *27*, 111–121, doi:10.1007/s00468-012-0774-8.
83. Krám, P.; Oulehle, F.; Štědrá, V.; Hruška, J.; Shanley, J.B.; Minocha, R.; Traister, E. Geoecology of a Forest Watershed Underlain by Serpentine in Central Europe. *Northeast. Nat.* **2009**, *16*, 309–328, doi:10.1656/045.016.0523.
84. O'Neill, A.L.; Kupiec, J.A.; Curran, P.J. Biochemical and Reflectance Variation throughout a Sitka Spruce Canopy. *Remote Sens. Environ.* **2002**, *80*, 134–142, doi:10.1016/S0034-4257(01)00294-2.
85. Hovi, A.; Raitio, P.; Rautiainen, M. A Spectral Analysis of 25 Boreal Tree Species. *Silva Fenn.* **2017**, *51*, doi:10.14214/sf.7753.
86. Rautiainen, M.; Lukeš, P.; Homolová, L.; Hovi, A.; Pisek, J.; Mõttus, M. Spectral Properties of Coniferous Forests: A Review of In Situ and Laboratory Measurements. *Remote Sens.* **2018**, *10*, 207, doi:10.3390/rs10020207.
87. Wu, Q.; Song, C.; Song, J.; Wang, J.; Chen, S.; Yu, B. Impacts of Leaf Age on Canopy Spectral Signature Variation in Evergreen Chinese Fir Forests. *Remote Sens.* **2018**, *10*, 262, doi:10.3390/rs10020262.
88. Rock, B.N.; Hoshizaki, T.; Miller, J.R. Comparison of in Situ and Airborne Spectral Measurements of the Blue Shift Associated with Forest Decline. *Remote Sens. Environ.* **1988**, *24*, 109–127, doi:10.1016/0034-4257(88)90008-9.
89. Campbell, P.K.E.; Rock, B.N.; Martin, M.E.; Neefus, C.D.; Irons, J.R.; Middleton, E.M.; Albrechtova, J. Detection of Initial Damage in Norway Spruce Canopies Using Hyperspectral Airborne Data. *Int. J. Remote Sens.* **2004**, *25*, 5557–5584, doi:10.1080/01431160410001726058.
90. Marín, S. de T.; Novák, M.; Klančnik, K.; Gaberščik, A. Spectral Signatures of Conifer Needles Mainly Depend on Their Physical Traits. *Pol. J. Ecol.* **2016**, *64*, 1–13, doi:10.3161/15052249PJE2016.64.1.001.
91. Misurec, J.; Kopacková, V.; Lhotakova, Z.; Albrechtova, J.; Hanus, J.; Weyermann, J.; Entcheva-Campbell, P. Utilization of Hyperspectral Image Optical Indices to Assess the Norway Spruce Forest Health Status. *J. Appl. Remote Sens.* **2012**, *6*, 063545, doi:10.1117/1.JRS.6.063545.
92. Hernández-Clemente, R.; Navarro-Cerrillo, R.M.; Zarco-Tejada, P.J. Carotenoid Content Estimation in a Heterogeneous Conifer Forest Using Narrow-Band Indices and PROSPECT+DART Simulations. *Remote Sens. Environ.* **2012**, *127*, 298–315, doi:10.1016/j.rse.2012.09.014.
93. Kováč, D.; Malenovský, Z.; Urban, O.; Špunda, V.; Kalina, J.; Ač, A.; Kaplan, V.; Hanuš, J. Response of Green Reflectance Continuum Removal Index to the Xanthophyll De-Epoxidation Cycle in Norway Spruce Needles. *J. Exp. Bot.* **2013**, *64*, 1817–1827, doi:10.1093/jxb/ert069.
94. Kokaly, R.F.; Asner, G.P.; Ollinger, S.V.; Martin, M.E.; Wessman, C.A. Characterizing Canopy Biochemistry from Imaging Spectroscopy and Its Application to Ecosystem Studies. *Remote Sens. Environ.* **2009**, *113*, S78–S91, doi:10.1016/j.rse.2008.10.018.
95. Ollinger, S.V. Sources of Variability in Canopy Reflectance and the Convergent Properties of Plants: Tansley Review. *New Phytol.* **2011**, *189*, 375–394, doi:10.1111/j.1469-8137.2010.03536.x.
96. Cescatti, A.; Zorer, R. Structural Acclimation and Radiation Regime of Silver Fir (*Abies Alba* Mill.) Shoots along a Light Gradient: Shoot Structure and Radiation Regime. *Plant Cell Environ.* **2003**, *26*, 429–442, doi:10.1046/j.1365-3040.2003.00974.x.
97. Kubínová, Z.; Janáček, J.; Lhotáková, Z.; Šprtová, M.; Kubínová, L.; Albrechtová, J. Norway Spruce Needle Size and Cross Section Shape Variability Induced by Irradiance on a Macro- and Microscale and CO2 Concentration. *Trees* **2018**, *32*, 231–244, doi:10.1007/s00468-017-1626-3.